Applications for assessing sediment sources in back-barrier systems

A Thesis Presented

By

CAROLINE G. LADLOW

Submitted to the Graduate School of the

University of Massachusetts Amherst in partial fulfillment

of the requirements for the degree of

MASTER OF SCIENCE IN GEOLOGY

September 2019

Department of Geosciences Master of Science in Geosciences

Applications for assessing sediment sources in back-barrier systems

A Thesis Presented

By

CAROLINE G. LADLOW

Approved as to style and content by:

Jonathan D. Woodruff, Chair

Timothy L. Cook, Member

Jeffrey M. Salacup, Member

Brian C. Yellen, Member

Julie Brigham-Grette, Department Head

Department of Geosciences

ABSTRACT

APPLICATIONS FOR ASSESSING SEDIMENT SOURCES IN BACK-BARRIER SYSTEMS

MAY 2019

CAROLINE LADLOW, B.S., LAFAYETTE COLLEGE

M.S., UNIVERSITY OF MASSACHUSETTS AMHERST

Directed by: Professor Jonathan D. Woodruff

In order to improve our understanding of present and future coastal environmental change, we look into the past using sediment that accumulates in coastal environments. We have done this for two disparate systems: a back-barrier lagoon in southwestern Japan, and freshwater tidal marshes along the Hudson River, New York, USA. In Japan, we used a 2,500-year sediment record to investigate coastal flood risk from tsunamis and typhoons. This is a critical area of study to better understand the spatial and temporal variability of these hazards in Japan. In the Hudson River we looked at modern (since 1800) deposition of sediment in anthropogenically constructed embayments that have formed tidal wetlands in the last few centuries. A better understanding of the factors that have attributed to these successful tidal marsh systems in the past can help inform future management decisions in the face of future sea level rise. Studying the history of coastal systems using the sediment record is a valuable tool for assessing hazard risk and habitat loss in the present and future.

LIST OF FIGURES

Figure Page

LIST OF TABLES

Table Page

TABLE OF CONTENTS

CHAPTER 1

A FLUVIALLY DERIVED FLOOD DEPOSIT DATING TO THE KAMIKAZE TYPHOONS NEAR NAGASAKI, JAPAN

1.1 Abstract

Previous studies in western Kyushu revealed prominent marine-derived flood deposits that date to the late-13th century and are interpreted to be a result of two legendary typhoons linked to the failed Mongol invasions of Japan in 1274 and 1281. The regional persistence and prominence of sediments dating to these "Kamikaze" typhoon events (meaning divine wind), raise questions about the origins of these late-13th century deposits. This is due in part to uncertainty in distinguishing between tsunami and storm induced deposition. To provide additional insight into the true cause of prominent late-13th century flood deposits in western Kyushu, we present here a detailed assessment of an additional event deposit dating from the late-13th century from Lake Kawahara near Nagasaki, Japan. This particular deposit thickens landward towards the primary river flowing into Lake Kawahara and exhibits anomalously high Ti:Sr ratios that are consistent with a fluvial rather than a marine sediment source. When combined with previous reconstructions, results support the occurrence of an extreme, late-13th century event that was associated with both intense marine- and river-derived flooding. Results therefore contribute to a growing line of evidence for the Kamikaze typhoons resulting in wide-spread flooding to the region, rather than the late-13th century deposit being associated with a significant tsunami impact to western Kyushu.

1.2 Introduction

The shorelines of Japan experience extreme coastal flooding from both seasonal typhoons and episodic tsunami events (Komatsubara and Fujiwara, 2007; Sasaki and Yamakawa, 2007; Suzuki et al., 2008). There are significant restrictions when assessing spatially varying flood risk from these two separate hazards, however, due to limited observations of their extremes within short instrumental records (e.g. Goto et al., 2017; Suppasri et al., 2013; Woodruff et al., 2013a). Prior to the onset of the best-track data set of typhoons in the Northern West Pacific in the mid-twentieth century (Chu et al., 2002), one must rely on historical records and natural archives of coastal flooding to constrain flood risk across Japan. The magnitude and impact of the most recent tsunami to strike Japan, the 11 March 2011 Tōhoku tsunami, greatly exceeded prior expectations at the time of the event (Japan Meteorological Agency, 2013), underscoring the importance and impact that additional insight from the historical record could offer. Quantifying risks and spatial variations associated with typhoons and tsunamis across Japan is an essential part of hazard preparation and planning (e.g. Normile, 2011; Goslin and Clemmensen, 2017).

Examples for compilations of historical records and natural archives of coastal flooding in Japan include Goslin and Clemmensen (2017), Nakata and Kawana (1995), and Watanabe (2001). Historical documentation of tsunamis and typhoons in Japan extends back at least several hundred years, but significant uncertainty associated with these early records limits their utility in improving flood risk assessments (Kortekaas and Dawson, 2007; Morton et al., 2007). Natural archives of flooding preserved within the geologic record are frequently used to independently validate early historical flood accounts. For example, overwash deposits from high-energy flood events that are preserved within the sedimentary sequences of coastal environments, such as those from back-barrier lakes and marshes, can be used to reconstruct pre-instrumental tsunami and typhoon frequency and intensity (e.g. Komatsubara and Fujiwara, 2007; Komatsubara et al., 2008; Chagué-Goff et al., 2012; Wallace et al., 2014; Brandon et al., 2015; Baranes et al., 2016, 2018; Chaumillon et al., 2017). The sandy overwash deposits left by both tsunamis and typhoons can often have very similar characteristics including being composed of coarse-grained beach material, exhibiting a lateral thinning landward, and containing elemental signatures consistent with marine-derived sediments. Though it is difficult to unambiguously differentiate between storm and tsunami overwash deposits preserved in back-barrier environments, distinguishing between these types of event layers is important because of the need to separately quantify the risks associated with both storms and tsunamis (Nanayama et al., 2000; Kortekaas and Dawson, 2007; Morton et al., 2007; Komatsubara et al., 2008; Sawai et al., 2009). Especially in countries like Japan with longer written historical records, pairing event deposits to historical documentation can help circumvent the uncertainty between deposits left by these coastal flooding hazards (Nanayama et al., 2000; Goff et al., 2004; Kortekaas and Dawson, 2007; Morton et al., 2007; Goto et al., 2015).

The subjectivity of historical accounts of natural disasters often raises questions about the reliability and accuracy of the descriptions of these events. For example, legend states that the two failed attempts by the Mongol Empire to invade Japan, first in 1274 and again in 1281, were prevented by the timely intervention of two intense typhoons. Now known as the Kamikaze typhoons, meaning ‘divine wind’, the storms were believed to be an intervention from the gods to protect Japanese sovereignty from the Mongols (Neumann, 1975; Rossabi, 2009; Sasaki, 2015). The historical significance of these typhoons leaves them susceptible to exaggeration over time, as the Mongols emphasized the storms as the reason it was impossible for their invasions to succeed, and Japan highlighted the storms as divinely sent to protect their nation’s sovereignty. The occurrence of two intense typhoons striking Japan within only 7 years is also inconsistent with the substantially lower average reoccurrence rate for typhoon landfalls in the region based on the modern instrumental record (Woodruff et al., 2015). Despite the potential for exaggeration and inconsistencies with modern typhoon climatology, natural archives and recent archeological observations support the occurrence of the Kamikaze typhoons. Evidence includes the recent discovery of sunken Mongol ships from the second invasion in Takashima Island and Imari bay (Kimura et al., 2014; Sasaki, 2015) and geologic evidence of contemporaneous overwash deposits in western Kyushu (Woodruff et al., 2009, 2015). Depositional evidence of the Kamikaze typhoons stems from prominent event deposits at Lakes Daija and Kamikoshiki (Fig. 1), with both sites preserving deposits from a marine-sourced flood event consistent with the timing of the two failed Mongol invasions (Woodruff et al., 2009, 2015). A tsunamigenic cause for these deposits could not be ruled out, however, due to similarities in deposition by tsunami- and typhoon-induced coastal flooding. Western Kyushu is largely considered to be at low risk of tsunamis relative to other regions of Japan, but this risk could be greater than current perception should the 13th century deposit be tsunamigenic in origin. Further research is therefore warranted to both confirm the regional persistence of the late-13th century deposits, as well as to help identify these events as either typhoon or tsunamigenic in origin.

Here we present a new sedimentary record from Lake Kawahara, a coastal lake in western Kyushu, to provide further insight regarding the history of extreme flooding in southwestern Japan and the underlying cause of the late-13th century deposits observed at the Daija and Kamikoshiki. The Kawahara site is significant because of its sensitivity to both coastal overwash and river flooding, and the potential to use concurrent rainfall-induced river flooding and coastal overwash flooding to delineate typhoon-induced deposition from strictly coastal flooding during tsunami inundation.

1.3 Site Description

Lake Kawahara is a small, coastal, and presently eutrophic lake on the inland side of the Nagasaki Peninsula, approximately 40 and 80 km north of Lakes Daija and Kamikoshiki, respectively (Fig. 1, 32.62 N, 129.83 E). The lake has a 13 ha (0.013 km^2) surface area, a maximum depth of 9 m, and a thermally stratified water column from February to October each year (Furumoto et al., 1999). The barrier beach is composed of fine to coarse sand and gravel and is approximately 250 m long, 130 m wide, and 7-10 m above mean sea level (MSL). A small inlet through this barrier beach on its southeastern end has resulted in an ephemeral connection between the lake and the ocean. A small high-gradient river empties into the western end of Lake Kawahara and drains a high-relief watershed of 1.4 km^2 with a maximum elevation of 330 m (Fig. 1). The bedrock within the watershed is primarily Cretaceous metamorphic schist, bordered by ultramafic rocks (Geological Survey of Japan, 2017). Sea level has remained relatively stable in the region over the past few millennia with a rise of approximately 50 cm since 4100 years BP (Yokoyama et al., 1996, 2012; Sato, 2001). The area is also tectonically stable relative to other regions of Japan closer to active faults (Nakada et al., 1994; Fukumoto, 2011).

Since 1945, only three typhoons at or above Category 3 intensity (Simpson and Saffir, 1974) have occurred within 90 km of Lake Kawahara: Typhoon Jean in 1965 as a Category 4 storm; Typhoon Bart in 1999 at Category 3 intensity; and Typhoon Leepi in 2015 as a Category 3 event (Fig. 1). Each of these typhoons made landfall to the south of Lake Kawahara, closer to the previously studied Daija and Kamikoshiki sites. No tsunamis have impacted western Kyushu with the exception of a localized tsunami event in 1792 caused by a volcanic dome collapse and resulting landslide internal to Shimabara bay and located to the east of the Kawahara site (Hoshizumi et al., 1999) (Fig. 1). The area surrounding the lake has been modified heavily in recent decades in part to mitigate against typhoon impacts. This includes the construction of a seawall that now armors the beach and several jetties near the outlet of the lake. Additionally, Lake Kawahara was historically brackish but a pump was installed in 1974 to remove saltwater from the lake and a sluice gate was installed at the inlet in 1979 (Hossain et al., 2013). Due to coastal fortification and modifications to Lake Kawahara, is it likely that the site is less sensitive to recording coastal flooding within sediments spanning the instrumental period (1945 CE to present); however, the sluice gate and recent pumping of the lake may provide a modern example for the transition from salt to fresh analogous to past natural closures of the barrier beach inlet.

1.4 Methods

Primary core locations from the deeper part of Lake Kawahara were chosen using bathymetry data collected with a 10 kHz echo-sounder (Kurnio and Aryanto, 2010), and subsequently cored using a modified Vohnout-Colinvaux piston corer (Baranes et al., 2016). Initial bathymetric mapping and coring were completed in November 2010, and supplementary surface cores at the same locations were collected in July 2014. Primary cores KAW5 (32.62311°N, 129.832°E), KAW2 (32.62334°N, 129.83264°E), and KAW4 (32.62356°N, 129.83316°E) lie along a shore-normal transect with a spacing of approximately 60-70 m (Fig. 1). Multiple, overlapping drives were collected from each core location in order to recover a continuous sequence. Additional discrete surface sediment samples from the riverbed and the beach were collected to characterize allochthonous sediments from fluvial- and marine-derived sources, respectfully. The central core (KAW2) was selected for constructing a detailed depth-to-age model based on ^{14}C and ^{137}Cs age constraints (Pennington et al., 1973; Ritchie and McHenry, 1990; Reimer et al., 2013).

After collection, all cores and discrete surface samples were shipped to the University of Massachusetts (Amherst, MA, USA) and stored at 4°C. Cores were opened using a Geotek core splitter followed by a complete visual description. Bulk geochemistry of cores and discrete surface samples was evaluated using an ITRAX x-ray fluorescence (XRF) core scanner (Croudace et al., 2006) with a molybdenum (Mo) tube operating at 30kV and 55mA and a ten second exposure time. The ITRAX core scanner also provided high-resolution x-radiograph images of relative density, which has proven particularly effective in initially identifying anomalously dense event deposits within cores (e.g. Woodruff et al., 2009, 2015). The ITRAX measures the relative abundances of a wide variety of elements. For the Kawahara cores however, particular attention was paid to variability in the relative abundance of titanium (Ti), strontium (Sr), and sulfur (S). Ti and Sr are commonly associated with terrigenous- (Peterson et al., 2000; Haug et al., 2001; Peterson and Haug, 2006) and marine- (Bowen, 1956; Chen et al., 1997; Chagué-Goff, 2010; Croudace and Rothwell, 2015) derived sediments, respectively, such that rises and peaks in the ratio of Ti:Sr could potentially represent an increase in terrigenous relative to marine sediment delivery. Elemental sulfur has been used to assess fluctuations in lake salinity associated with past inlet-connectivity to the sea, with higher S indicating higher salinity (Chagué-Goff, 2010; Sato, 2001; Croudace and Rothwell, 2015; Casagrande et al., 1977).

Following scanning with the non-destructive ITRAX core scanner, identified event deposits and background sediments were sub-sampled at 1cm intervals for grain size. All grain size samples were treated twice with 30% hydrogen peroxide to remove organic material following methods described by (Triplett and Heck, 2013). Grain sizes were obtained using a Beckman Coulter LS 13 320 laser diffraction particle size analyzer with a range of 0.04 µm to 2000 µm.

Ages of recent sediments were determined based on identification of the 1954 onset and 1963 peak in ^{137}Cs activity associated with atmospheric testing of nuclear weapons (Pennington et al., 1973), and measured using a Canberra GL2020R low-energy germanium detector. Age control points below the onset of ^{137}Cs were obtained based on radiocarbon (^{14}C) analysis of terrestrial macrofossils (leaves and seeds) subsampled from KAW2. Macrofossils were cleaned with deionized water, dried, and shipped to the National Ocean Science Accelerator Mass Spectrometry (NOSAMS) center in Woods Hole, MA for analysis. All provided radiocarbon ages were converted to calendar years BP (years before 1950 CE), using IntCal13 (Reimer et al., 2013). Both the ^{137}Cs and radiocarbon dating results were used to create a Bayesian-derived depth-to-age model with associated uncertainties using the Bchron software package (Haslett and Parnell, 2008; Parnell et al., 2008).

1.5 Results

1.5.1. Bulk geochemistry of river and beach surface samples:

Sr and Ti counts for discrete samples from the barrier beach and primary freshwater stream are evaluated to assess the validity of Ti:Sr as a proxy for terrigenous material enrichment in Lake Kawahara sediments. Ti counts for the river sample were roughly fourteen times that measured for beach sediments, while Sr counts are approximately three times higher in the beach sample than in the river sample (Fig. 2). Therefore, similar to previous results (e.g. Baranes et al., 2016), resultant Ti:Sr ratios are elevated substantially for fluvial-derived material when compared to those with a marine source at Kawahara.

1.5.2. Visual, Physical, and Chemical Characteristics of Sediment Cores:

The three primary cores KAW5, KAW2, and KAW4 extend to a depth of 377 cm, 540 cm, and 295 cm below the sediment-water interface, respectively. Each core is composed primarily of fine-grained silt and clay, with no sand present, and can be split into three primary lithologic units based on texture, composition, color, and bedding characteristics (Fig. 3). The lower unit in all cores is composed of brown-grey mud and extends from the base of KAW5, KAW2, and KAW4 up to a depth of 245, 280, and 270 (Fig. 3). For the two deeper cores this lower unit contains subunits of darker grey mud at intervals of 260-306 cm in KAW5 and 355-385 cm in KAW2. The intermediate unit in all cores consists of heavily laminated brown-grey mud extending between 150-245 cm, 150-280 cm and 165-270 cm in KAW5, KAW2, and KAW4. This is with the exception of a break in lamination in the intermediate unit in KAW4 between 200-245 cm. An upper unit extends from 0-150 cm in KAW5 and KAW2, and 0-165 cm in KAW4, and is primarily composed of organic-rich black-grey mud and black gyttja, with a section of laminated muds in between. The upper unit of KAW4 extends down into the brown-grey mud of the intermediate unit, and the delineation between these units is based on the absence of laminations and the decrease in S. The thickness of the laminated section varies across the transect, from 30-40cm in KAW5 and KAW4, and 30-55cm in KAW2. Anomalous event deposits in Lake Kawahara appear as high-density layers in the x-radiographs and were also apparent upon visual inspection as light-grey-to-white clay deposits. KAW5 only contains one such prominent deposit from 210-216cm (6 cm thick), KAW2 has two such deposits from 212-215cm (3 cm thick) and 486-487cm (<1 cm thick), and KAW4 contains two very thin (<1cm) deposits between 200-250cm (Fig. 3). The event deposits at 210 cm in KAW5, 212 cm in KAW2, and 223 cm in KAW4 appear correlative and represent a unique, basin-wide depositional event not repeated elsewhere in the record. Across the core transect, median grain sizes in the deposit for inorganic sediments ranged from 15.7-19.3 μm and did not exhibit much in terms of distinguishable spatial trends. Clastic material within background sedimentation above and below the deposit were comparable in size, with a median grain sizes range of 15.0-to-31.7 μm (Table 1).

The XRF results for primary core sites exhibit patterns that broadly coincide with the three different lithologic units (Fig. 3). The lower unit has relatively high levels of S and low Ti:Sr ratios that remain fairly constant throughout the unit. There does not appear to be a substantial increase or decrease in S or Ti:Sr at the boundary between the lower unit and intermediate unit, but the top of the intermediate unit shows an up-core increase in Ti:Sr and a rapid step-function decrease in S. The transition from the intermediate to upper unit at ~150 cm is particularly evident: all cores show a sudden drop in elemental S and a doubling in Ti:Sr that begins in the upper portion of the intermediate unit. All three cores also show elevated S abundances that coincide with the heavily laminated sediments both in the intermediate unit, and near the surface at roughly 30-50 cm depth. Following the rise in S at ~50 cm in the upper laminated unit is relatively rapid up-core decline at approximately 30 cm in all three cores and the disappearance of laminations. This transition to unlaminated sediments is followed by an increase in Ti:Sr within the uppermost 5-10 cm.

The unique, high-density event deposit at 210 cm in KAW5, 212 cm in KAW2, and 223 cm in KAW4 are all located directly below the rapid up-core drop in S and based on this stratigraphic marker are consistent with being deposited concurrently (Fig. 3). This unique, high-density event deposit identified in all three cores is associated with peaks in both S and Ti:Sr (Fig. 4). The peak in Ti:Sr is most pronounced in the most landward core KAW5, and observed to decrease in relative value for the middle KAW2 core, and followed by the lowest spike in Ti:Sr in the most seaward KAW4 core. A similar seaward decrease is observed in the thickness of this deposit, with a maximum thickness of 6 cm at KAW5, a thickness of 2-3 cm in KAW2, and a thickness of less than 1 cm in KAW4 (Fig. 4).

1.5.3 Age Model:

The five radiocarbon (^{14}C) ages and the modern Cesium (^{137}Cs) age constraints from KAW2 are all chronologically consistent (Table 2). Based on ^{14}C ages the 540 cm core extends back to approximately 2,500 years BP. The slope of the median age line of the depth-to-age model suggests a relatively steady accumulation rate of 1.5-2.1 mm/yr from the base of the core at 540 cm up to the youngest ^{14}C age at 178.5 cm and extending through both the lower and intermediate lithologic units. The accumulation rate increases to approximately 4 mm/yr somewhere between the youngest ^{14}C age at 178.5cm and the onset for ^{137}Cs at 39cm near the basal extent of the upper lithologic unit. The modern chronological constraints for the onset and peak of ^{137}Cs are consistent with an average accumulation rate of roughly 7mm/yr and are the highest in the core. Applying this modern accumulation rate to recent sediments dates the most up-core recent drop in S at 30 cm to the early 1970's (Fig. 5). The prominent deposit at 212 cm in KAW2 falls within older sediment below the observed rise in accumulation rate above 178.5cm. The depth-to-age model derived 2-sigma age range for this event deposit is 1155-1487 CE, with a median age of 1321 CE (Fig. 5).

1.6 Discussion and Interpretation

The transect of cores from Lake Kawahara display three fine-grained lithologic units that likely represent periods of varying degrees of connectivity to the ocean, as shown by the counts of Ti:Sr and S (Fig. 3). The up-core decrease in S at 30 cm (Fig. 5) is concurrent with the installation of the pump and sluice gate in the 1970s to de-salinize the lake, supporting S as a qualitative proxy of salinity in Lake Kawahara, and consistent with past studies (e.g. Croudace and Rothwell, 2015; Boyle, 2000; Sato, 2001; Haug et al., 2003; Chagué-Goff et al., 2012). Additionally, periods of elevated S at Kawahara are largely coincident with the higher preservation of laminations. The lower and intermediate units across the cores have relatively depleted Ti:Sr and elevated S, suggesting a more open connection to the ocean during this time and an increase influx of marine-sourced material. The intermediate unit contains the greatest preservation of laminations across all three cores, which is indicative of the salinity-induced stratification of the water column and resulting anoxic-bottom waters in the lake. The upper unit of all three cores show depleted S and elevated Ti:Sr, which together signify less marine connectivity and an enrichment in fluvial sedimentation relative to marine. The transition between the intermediate and upper units around 1600 CE (~150 cm depth) indicate that the inlet was likely closed off to the ocean at this time, cutting off the majority of marine seawater and sediments.

Lake Kawahara sediments lack modern flood deposits for comparison to paleo-deposits (likely due to the fortification of the beach and man-made closure of the barrier inlet in recent decades), and exhibit evidence for sudden shifts in environment and the level of connectivity of the lake to the sea. Both of these factors make it difficult to assemble a complete flood reconstruction through the full 2500-year sedimentary record obtained from the lake. However, the prominent event layer identified in all three cores stands out as a unique depositional event within the lower and intermediate units, spanning an interval of 900 years from 1,600-2,500 CE. The high-density signature of this deposit is consistent with a higher mineralogic content relative to surrounding sediment, which could have been sourced from either fluvial input of terrestrial material or overwash transport of beach sediment (Fig. 4). At Lake Kawahara, this event deposit is fine-grained (15-19 µm) and thickens landward which is consistent with flooding from the river (Wright, 1977; Cook et al., 2015). In contrast, marine overwash deposits typically thin landward and are coarse-grained (Nanayama et al., 2000; Morton et al., 2007; Komatsubara et al., 2008). Additionally, the cores also show that this Kawahara deposit is elevated in Ti:Sr (Fig. 4), which in turn points to an enrichment in fluvial rather than marine sediments (Fig. 2). The KAW2 depth-to-age model reveals that this prominent flood occurred between 1155-1487 CE (95% age range) and is consistent with the timing of the Kamikaze typhoons in 1274 and 1281 and the age of prominent marine overwash deposits previously identified in Lakes Daija and Kamikoshiki. Of the Kamikaze events the 1281 typhoon is generally considered to be of greater intensity (Turnbull, 2013). Therefore, we attribute the single late-13th century Kawahara deposit to the later of the two Kamikaze events in 1281 (although it is also possible that the deposit could be combined deposition from the 1274 and 1281 events).

The elemental signature, high density, and landward thickening of the most prominent deposit at Kawahara all support the occurrence of a 13th century extreme precipitation event that overlaps in time with the prominent marine-flood deposits previously identified at Daija and Kamikoshiki. Collectively, these results point to the occurrence of anomalous flooding from both the land and sea during the timing of the failed Mongol invasions, thereby strengthening the evidence for the occurrence of the Kamikaze typhoons. The more prominent fluvial deposit at Lake Kawahara when compared to predominant marine deposits at Daija and Kamikoshiki could be due to a number of factors, including: 1. the barrier at Kawahara being substantially higher (~10 m) than the barrier beaches at the other two sites (between ~2-4 m), 2. the watershed of Kawahara being over twice the size of that at Kamikoshiki and Daija, and 3. the storm tracks for the 1281 event passing between the more northerly Kawahara site and the more southerly Daija and Kamikoshiki sites such that the front right quadrant of the storm where coastal flooding is enhanced passed over the two southern sites (Landsea et al., 2004; Brandon et al., 2013), while the left side of the storm with potentially greater precipitation passed over the Kawahara site.

Mechanisms other than extreme precipitation exist that could potentially explain the terrestrially derived deposit at Kawahara. For instance, earthquakes accompanying tsunamis could result in landslides that would increase the sediment output from regional rivers (e.g. Milliman and Farnsworth, 2011). However, relative to the rest of Japan the area around Kawahara is depleted in active tsunamigenic faults (Yokoyama et al., 1996; Taira, 2001). Further, an enclosed tsunami event generated by local fault sources and localized landslides are unlikely to cause a tsunami large enough in size to impact all three openly seaward facing sites mentioned in this study. Conversely, a tsunami derived from non-local sources such as the Nankai trough or the Ryukyu Islands would not be associated with local earthquake/landslides and in turn would be less likely to result in the terrestrially derived deposit observed at Kawahara. Goto et. al. (2017) showed evidence of a tsunami with a return flow back to the sea that resulted in deposition of both fluvial and marine sediments into the lagoon. Thus, a tsunami event of this nature is difficult to rule out completely as the cause of the regional deposit across western Kyushu, despite the evidence of the fluvial deposit observed at Kawahara. However, a tsunami large enough to impact all three sites in western Kyushu would likely have been mentioned in historical records, yet no such documentation for a significant tsunami event exists. In contrast, accounts of the Kamikaze typhoons indicate that these extreme floods were being documented in the late-13th century in the region. Thus, the prominent late-13th century fluvial deposit at Kawahara, when combined with historical accounts of the Kamikaze typhoons, and previously identified coastal flood deposits at Daija and Kamikoshiki dating to the same time period, all support the Kamikaze typhoons causing significant flooding in the region by both land and sea.

1.7 Conclusion

Prior results from Lake Daija and Kamikoshiki support the occurrence of late-13th century events associated with extreme coastal flooding in southwestern Kyushu. New analyses presented here from Lake Kawahara provide additional evidence for a late-13th century flood event. The modal age for the most prominent event deposit in Lake Kawahara is matched to the timing of the Mongol invasions, and the deposit can be traced continuously through the transect of cores. However, in contrast to evidence of marine flooding from Lake Daija and Kamikoshiki, the late-13th century deposit at Kawahara thins seaward, shows no significant grain size increase, and exhibits an enrichment in terrigenous material that increases when progressing towards the lake's primary freshwater tributary. The most prominent deposit from Lake Kawahara, therefore both dates to the timing of the Mongol invasions and supports significant freshwater flooding during the timing of at least one of the events. When combined with previous regional studies, preserved late-13th century event deposits from near the location of the Mongol invasions in 1274 and 1281 provide evidence for the two leading forms of typhoon-induced flooding (i.e. coastal and fluvial), and in turn contribute to a growing line of evidence for the occurrence of intense typhoons around the time of these invasions.

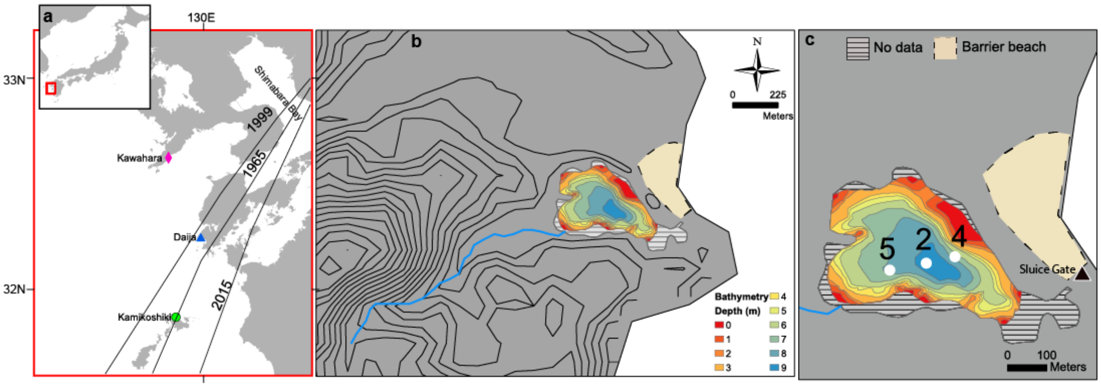

Figure 1 a) Regional map showing the location of Kawahara (diamond), along with other study locations referred to in the text (Daija-triangle, Kamikoshiki-circle), and the paths of best track Category 3 and greater typhoons within 90km of Lake Kawahara. b) Topographic map of Lake Kawahara watershed (black lines, 10m contour interval). The primary tributary draining into the lake enters from the southwest. c) Bathymetry (1m colored-contour interval) of Lake Kawahara and numbered core locations (note the order of cores across the transect). Hashed grey area of the lake has no bathymetry data, the light area with a dashed outline represents the location of the barrier beach, and the black triangle marks the location of the sluice gate constructed on the inlet along the site's barrier beach

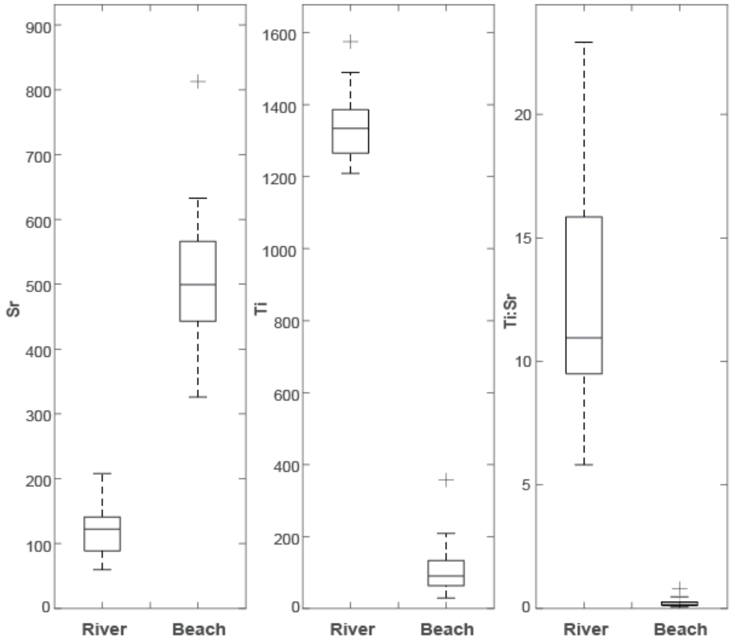

Figure 2 Relative concentrations of elemental strontium (Sr), titanium (Ti), and the ratio of Ti:Sr in discrete surface samples from the river and beach at Lake Kawahara. Each horizontal line in the box plot marks the 25th, 50th, and 75th percentile, with the whiskers extending to the maximum and minimum values that are not outliers, and then plus signs mark the outliers

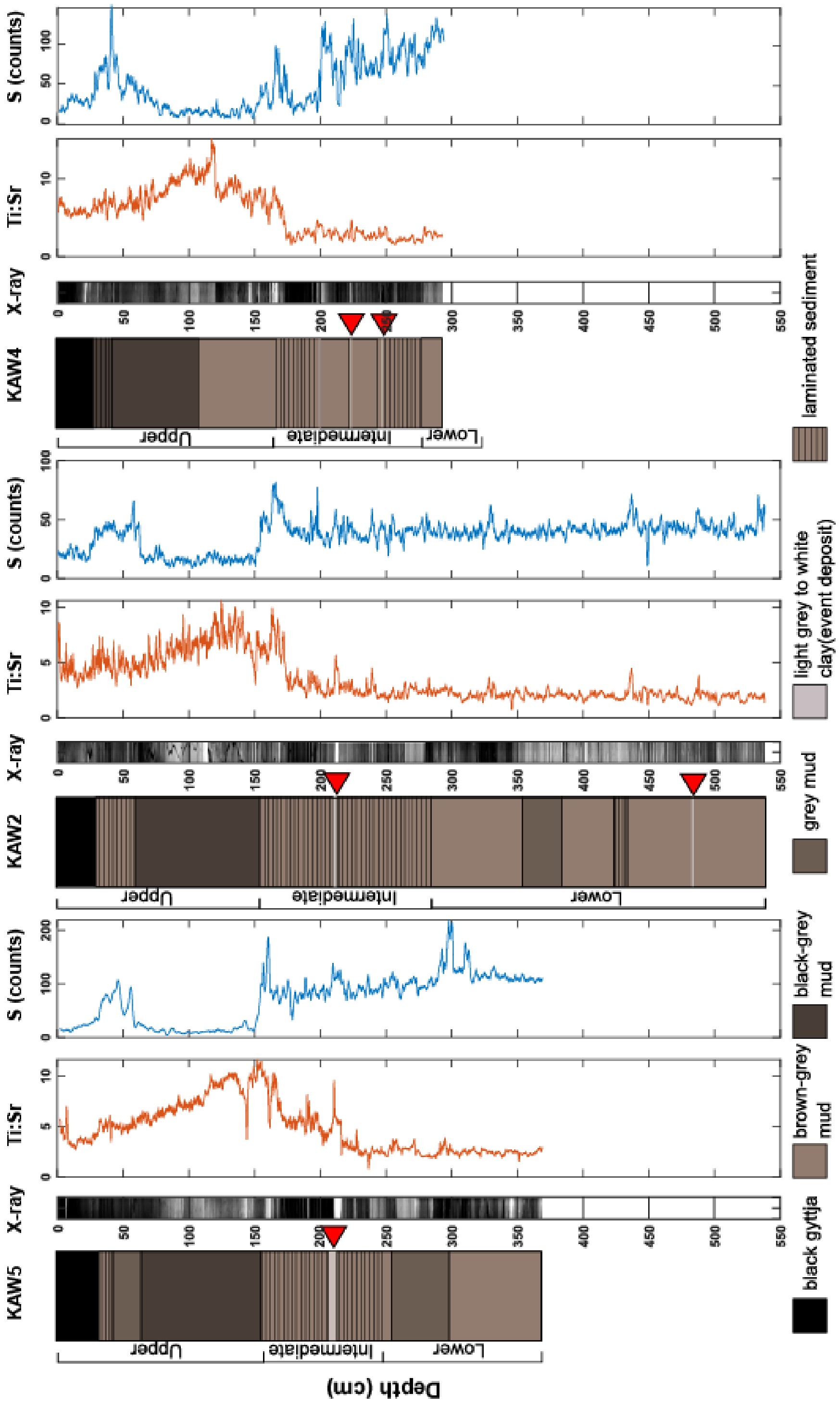

Figure 3 Depth profiles for the central transect of KAW5, KAW2, and KAW4 at Lake Kawahara (see Fig.1 for location). Note the order of cores 5, 2, and 4 go from landward to seaward. *From left to right for each core*: a graphic core description is pictured with the key below (the upper, intermediate, and lower unit of each core is delineated, and triangles delineate event deposit locations), the x-radiograph images with light bands indicating denser sediments, the Ti:Sr ratio, and relative abundance of S showing total counts

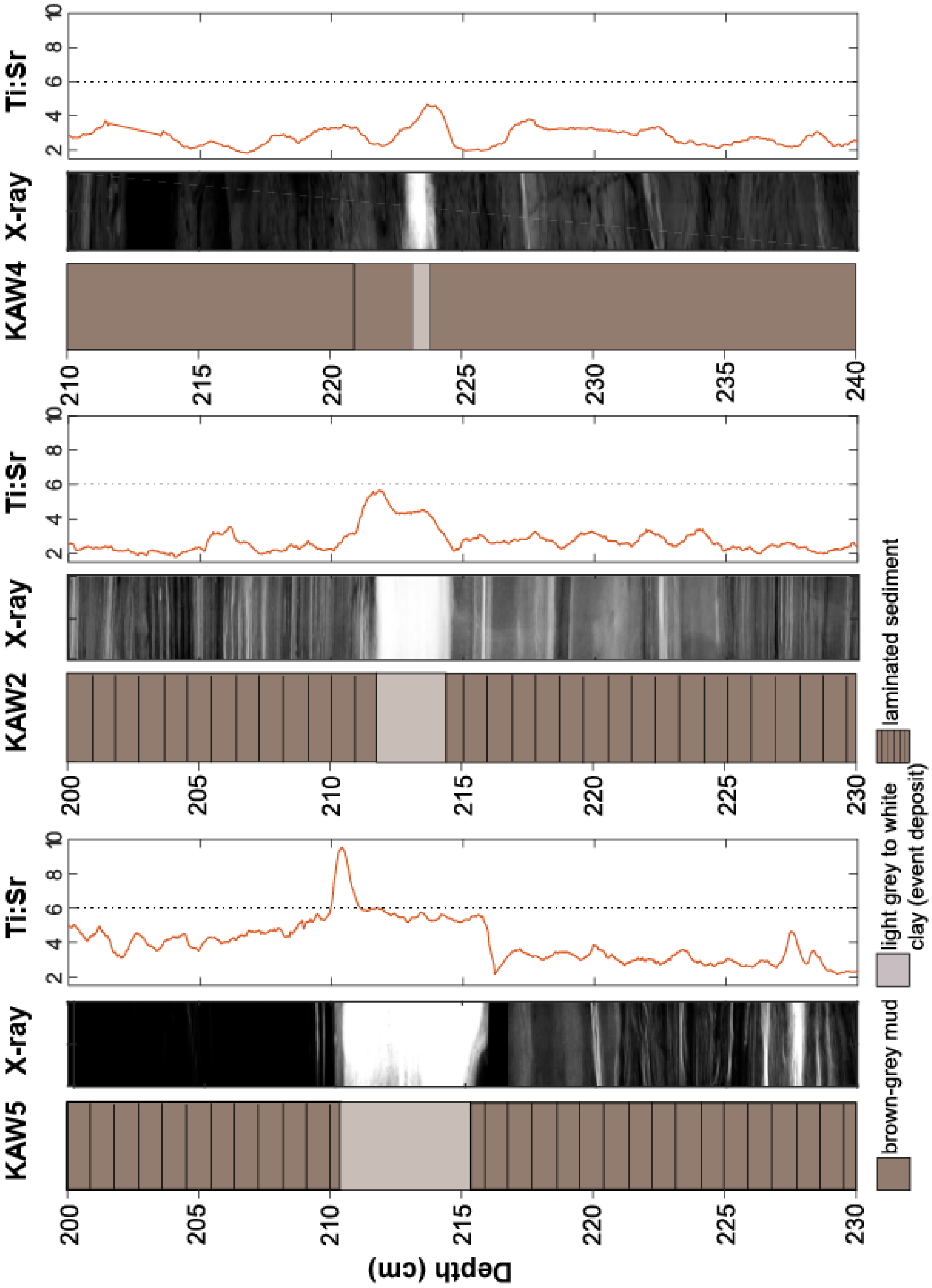

Figure 4 *Left to right*- 30 cm section of KAW5, KAW2, and KAW4 surrounding the most notable deposit at approximately 210cm depth. Presentation is similar to Fig. 3 showing first the graphic description for each core, followed by the core's radiographs, and the ratio of Ti:Sr. Dashed vertical line in Ti:Sr depth-profiles are all at 6 for reference. Note the different y-axis values for each core section and that the black lines are a graphic representation of the laminae rather than the actual lamination counts

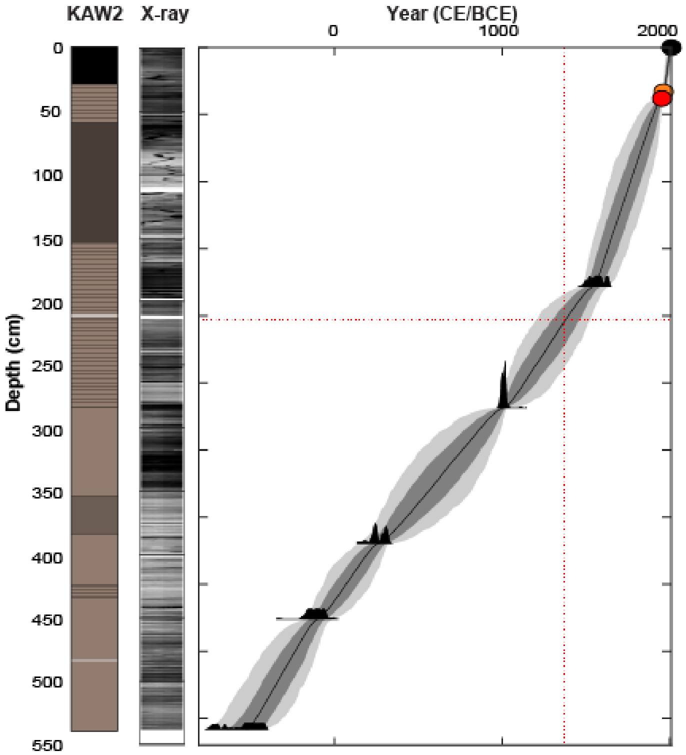

Figure 5 *Left:* from left to right: KAW2 core description, radiograph image, and the depth-to-age model constrained by radiocarbon ages (black filled curves) and the onset and peak in ^{137}Cs (red and orange circles, respectively). The black line designates the median age, while the light and dark grey filled regions show the 68 and 95 percent highest posterior density uncertainty ranges.

Below left: Age probability distribution for the most prominent event layer at 213 cm.

Below right: X-radiograph image of the top 40cm of KAW2, along with depth profiles of ^{137}Cs activity and S.

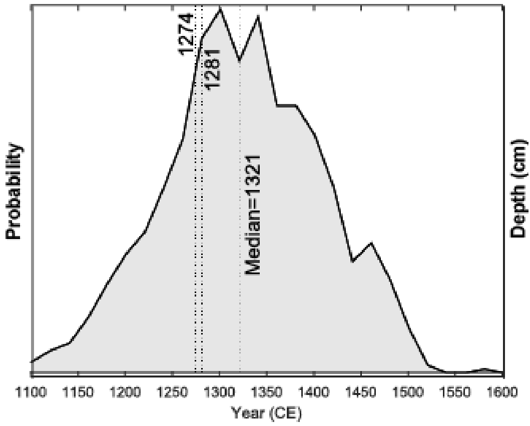

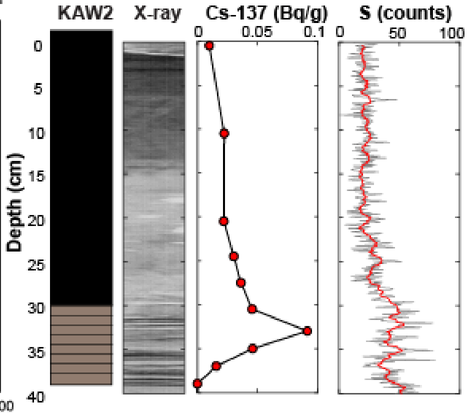

Table 1 Grain size results for the background sediments above, below, and within the most prominent event deposit. The numbers reported are an average of the median (D50) for each sample, the standard deviation of the samples, and *n* is the number of samples used for each average (a total of 30 samples in each core)

Core:	*KAW5* D50 (μm)	*KAW2* D50 (μm)	*KAW4* D50 (μm)
Above Deposit	15.7 ± 1.2 (n=8)	15.0 ± 1.8 (n=11)	19.4 ± 4.4 (n=16)
Deposit	16.9 ± 2.4 (n=7)	19.3 ± 2.4 (n=3)	15.7 (n=1)
Below Deposit	15.9 ± 2.0 (n=15)	15.8 ± 5.0 (n=16)	31.7 ± 9.6 (n=13)

Table 2 Radio carbon NOSAMS C-14 Lab numbers, sample depths, radiocarbon ages with uncertainties, and 1-sigma age ranges in years BP (Reimer et al., 2013) calibration

Lab Number	**Depth (cm)**	**Uncalibrated ^{14}C Age**	**Calibrated 1-sigma age ranges (Years BP)**	
OS-86784	178.5	325 ± 25	435	418
			413	353
			333	314
OS-86711	268.5	1020 ± 25	955	927
OS-86553	396.6	1780 ± 25	1727	1691
			1669	1626
OS-86570	426	2090 ±35	2004	2027
			2035	2073
			2076	2113
OS-86721	508.2	2430 ± 35	2678	2675
			2659	2644
			2607	2604
			2492	2362

CHAPTER 2

RAPID TIDAL MARSH DEVELOPMENT IN RESPONSE TO ANTHROPOGENIC SHORELINE MODIFICATION- HUDSON RIVER ESTUARY

2.1 Abstract

To improve the Hudson River Estuary's resilience to sea level rise, there are plans to create and restore marshes throughout its tidal reach. While there is evidence that humans have had negative impacts on marshes globally, there is an increasing awareness that some forms of modifications have actually created healthy tidal marshes along the tidal extent of the Hudson River. Here we present results from three inadvertent successful examples of marsh creation due to the emplacement of dredge spoils and the construction of piers and the railroad since the industrial era: Stockport Marsh, Tivoli Bays: North and South, and Esopus Marsh. For comparison, we present results from a marsh that long predates the industrial era and has been relatively unaffected by the changes to estuarine morphology. Sediment cores show that anthropogenic alteration of the flow conditions at these locations in the form of railroad causeways, dredge spoil islands, and jetties created low-energy areas with high sediment trapping efficiency. This allowed for the fast accumulation of sediment and the development of robust freshwater tidal marsh systems that have accreted at rates ranging from 0.8 to 1.5 cm per year, exceeding projected rates of sea level rise over the next century. These rapidly formed marshes can serve as models to guide future marsh restoration efforts in the Hudson River estuary.

2.2 Introduction

Wetlands and marshes provide society with valuable ecosystem services including storm protection, water purification, carbon sequestration, and many others (Craft et al., 2009; Barbier et al., 2011). Many natural tidal marshes in the northeastern United States have developed over the past few millennia since rates of sea level rise stabilized about 6,000 years ago (Redfield, 1972).

Marshes in Jamaica Bay (Queens, NY), Westport River, MA, and Chesapeake Bay are commonly used as examples of sediment starved systems that may not keep pace with accelerated sea level rise and climate change (Hartig et al., 2002; Sritrairat et al., 2012). The vulnerability of marshes to sea level rise (SLR), tides, and sediment supply creates a pressing need to understand the factors that influence the formation and health of marshes and wetlands. These factors have yet to be well-constrained, particularly in the less-studied freshwater tidal marshes and wetlands which are widespread on passive margins where prominent freshwater tidal reaches of river systems can often extend over 100 kilometers landward and are common to the eastern US. One of the longest tidal reaches observed for this region is within the Hudson River Estuary (Hudson River Estuary) (Tabak et al., 2016; "HRECRP," 2016). The Hudson River Estuary is highly channelized and fjord-like, with steeply sloping shorelines, fringed where possible by a relatively small and narrow floodplain.

The Hudson River Estuary was accepted into the National Estuary Program in 1988 and since then there have been efforts to create a comprehensive strategy for habitat restoration through a collaboration of federal, state, and local agencies. The objective for 'Wetlands' is to "create or restore 1,000 acres (4.05 kilometers^2) of wetlands by 2020… (and) a total of 5,000 acres (20.24 kilometers^2) by 2050" ("HRECRP," 2016). These goals involve an estimated \$3.5 billion USD on the wetland objective alone. Despite a concerted focus on tidal wetland restoration and growth in these most recent Hudson River Estuary Comprehensive Restoration Plans (HRECRP), many questions remain about how to best increase the extent and elevation of existing marshes. Models and projections of future wetland change explicitly acknowledge a lack of data for constraining accretion rates of marsh and mudflat systems particularly in freshwater systems (e.g. Tabak et al., 2016), and it remains unclear how wetland growth has and will continue to be impacted by changes in sea level, tides, and river discharge (e.g. Ralston et al., 2018; Wall et al., 2008; Kemp et al., 2017; Tabak et al., 2016; Nitsche et al., 2010). Thus, prior to these costly investments, an effort to constrain sedimentologic and hydrologic factors in addition to understanding previously successful wetland creation projects is needed. Future marsh restoration projects would benefit greatly from a better understanding of the conditions that have allowed for the evolution and development of existing tidal marshes factors that allow existing tidal marshes in the Hudson River Estuary. We define the Hudson River Estuary as the full tidal reach of the Hudson River.

The tidal regime and glacial over-deepening of the channel have resulted in very unique hydrologic and sediment dynamics, and the tidal marshes that grow along the riverbanks are of great interest now due to the aforementioned projects to create and restore marsh habitat. The primary upstream inputs to the Hudson River are the Mohawk and Upper Hudson Rivers, accounting for 70% of the freshwater and sediment source (Abood, 1974; Woodruff et al., 2001; Wall et al., 2008). Prior studies on a few of the Hudson River tidal marshes including Piermont Marsh, Iona Marsh, and Tivoli North Bay indicate that these systems are relatively stable and have persisted for millennia (Pederson et al., 2005; Chou, 2010; Sritrairat et al., 2012).

This study focuses on the Lower Hudson Basin, the tidal portion of the Hudson River south of Albany, NY (Wall et al., 2008) (Figure 6). Here, we will examine three marshes within these anthropogenically modified shorelines: Stockport Marsh, Tivoli Bays, and Esopus Marsh. For comparison, we will also present results from Iona, a Hudson River tidal marsh that has been studied previously (Chou, 2010).

2.3 Site Descriptions

The tidal stretch of the Hudson River from New York City at The Battery, up to Albany, NY has undergone major modifications in the last few hundred years. These alterations for shipping, recreation, and trade have dramatically altered the natural sedimentologic and hydrologic regimes. The Hudson River Railroad runs directly along the bank of the river from New York City to Albany, often crossing shallow embayments. The southern railroad section up to Peekskill, NY was constructed in 1849, and the northern section to Albany was constructed in 1851 (Aggarwala, 1993). Additionally, the river channel has been actively dredged since the 1800s to deepen the channel and allow for increased navigation (Ralston et al., 2018). Historical records suggest that the tidal range from 150 to 200 km north of The Battery is 1.2 m (this stretch includes Stockport, Tivoli, and Esopus), and near 80 km is approximately 0.8 m (the Iona site) (Ralston et al., 2018). For the purposes of this study, the entire tidal reach of the Hudson River will be referred to as the Hudson River Estuary. An assessment of the impacts of these anthropogenic modifications to the tidal marshes of the estuary has yet to be complete.

The historically braided, shallow upper estuary presented difficulties during the 19th century with navigation and transportation up to Albany. The federal government took control of Hudson River navigation projects in 1831, constructing a number of longitudinal dikes to constrict flow, and dredging to deepen the channel (Collins and Miller, 2012). These efforts were expanded repeatedly in 1867, 1925, and 1932 and compared to the modern extent over 1200 hectares (ha) of the total water area have been filled by dredge spoils during the 20th century (Collins and Miller, 2012). In 1819 the Hudson River average channel depth was just over 1 m, but since the 1930s has been maintained at about 9.7 m (Collins and Miller, 2012). The New York railroad section connecting New York City, Poughkeepsie and Albany was completed in 1851. Piers cutting across the channel to lighthouses and other features were also constructed throughout the 19th and 20th centuries, including the Saugerties lighthouses ("Timeline – Saugerties Lighthouse," 2011) (Figure 8).

The Hudson River National Estuarine Research Reserve has several marshes that are the focus of several studies. Three of the marshes in this study, Stockport, Tivoli Bays, and Iona are among these study sites, and Esopus is just three kilometers north of the Tivoli Bays at the outlet of a sediment-rich watershed. For consistency with prior studies, the locations of each site are in reference to their distance from The Battery in New York City.

2.3.1 *Stockport Marsh (SPM): 190 km north of The Battery*

Near Stockport, NY the Kinderhook and Claverack creeks join to form the Stockport Creek 2.5 km east of the Hudson River, draining a catchment area of 1300 km^2 (Table 3). Historical air photos and navigational charts indicate that dredge spoils were placed just south of the outlet of Stockport Creek during the early 1930s (Figure 7). The predominant vegetation type in this marsh is narrowleaf cattail (*Typha angustifolia).*

2.3.2 *Tivoli Bays: North (TVN) and South (TVS): 158 and 156 km north of The Battery*

Tivoli Bays Natural Heritage Area is comprised of a north and south embayment bound by the railroad trestle to the west and bedrock to the east. During the semi-diurnal tides water enters these two embayments through a series of culverts. The northern bay (Tivoli North, TVN) has developed into a full marsh and the southern bay (Tivoli South, TVS) remains a tidal mudflat (Figure 8). Each bay is located at the mouth of a small tributary, Stoney Creek at TVN, and Sawkill Creek at TVS, with catchments of similar areas of 60-70 km^2 (Table 5). The predominant vegetation at TVN is narrowleaf cattail (*Typha angustifolia)* and at TVS is non-native water chestnut (*Trapa natans*).

2.3.3 *Esopus Marsh (ESP): 160 km north of The Battery*

The Esopus marsh/delta complex lies approximately three kilometers north of the Tivoli Bays, and on the opposite side of the Hudson River at Saugerties, NY (Figure 8). The Esopus tributary drains a 1100 km^2 watershed with sub-catchments known for their relatively high regional sediment yields, resulting in a well-developed delta at its mouth (Table 5) (Yellen and Steinschneider, 2019). The channel for Saugerties Harbor was dredged and piers were built out to the lighthouse in 1888, dividing the marsh system into a northern and southern section ("Timeline – Saugerties Lighthouse," 2011). The main vegetation in the southern portion is the invasive common reed *(phragmites australis),* and in the northern section is the narrowleaf cattail (*Typha angustifolia)*. The marsh/delta complex is fringed along the shore by the seasonal development of non-native water chestnut (*Trapa natans*) in shoaling regions along the west side of the Hudson's main channel.

2.3.4 *Iona Island (INA): 72 km north of The Battery*

Iona Island Marsh is located on the west side of the Hudson River and approximately 90 km downstream of Tivoli Bays and Esopus (Figure 9). The main tributary to this marsh is Doodletown Brook, draining a watershed of 10 km^2 (Table 3). While the other marshes discussed here are entirely freshwater, Iona Island exhibits brackish conditions when freshwater discharge is low on the Hudson River and the salinity reach of the estuary extends beyond the site (Chou, 2010). While the railroad does intersect this marsh system, prior sediment cores from Iona suggest that the marsh has since approximately 4400 BCE, likely due to the presence of bedrock outcrops, including Iona Island, in this portion of the river (Chou, 2010). Additionally, there is a small causeway road built in the 1980s that runs out across the railroad track to some facilities on the eastern side of the railroad tracks. The primary vegetation at this site is narrowleaf cattail (*Typha angustifolia)*.

2.4 Methods

2.4.1 *Field methods and sampling*

This study is framed on assessing the development of representative wetland systems within the tidal reach of the Hudson River including three freshwater marshes (SPM, TVN, ESP), one brackish marsh (INA), and one mudflat (TVS) (Figure 6). The main coring strategy when possible was to collect cores across a transect from the tributary inlet to the outer edge of the marsh on the Hudson River. At Iona Island and Esopus Marsh, cores were taken where access was possible as the density of the vegetation made traversing the marshes difficult. A 200 MHz Mala ground-penetrating radar (GPR) was used initially to approximate the depth of sediment across the marsh. This was followed by a probing survey with a 2.5 cm diameter small gouge corer in order to confirm depth to basement material and to confirm targeted coring sites.

Cores in the marsh were primarily obtained using a 1-m long, 6.3 cm diameter gouge corer. When the gouge corer failed to recover poorly consolidated surficial sediments, the cores were collected using a shorter 0.5 m long, 5 cm diameter Russian peat corer for surface drives. Cores from Tivoli South were obtained using a modified Vohnout-Colinvaux piston corer with 4.8cm diameter, 2.2 m long polycarbonate barrels. Where possible, cores were taken at overlapping intervals to ensure continuous recovery (see Appendix: Table 6).

2.4.2 *Core splitting and descriptions*

Following collection, cores were brought to the University of Massachusetts (Amherst, MA, USA) and stored at 4°C. All piston cores were opened with a Geotek core splitter, while gouge cores were split and stored in 6 cm halved-PVC piping. For the gouge and piston coring methods an archive half was preserved, while the Russian peat corer provided a single half upon recovery. After opening, all cores were visually described for an initial qualitative assessment of down-core variability in gran size, organic content, cohesiveness, and color.

2.4.3 *X-ray fluorescence*

Each core was scanned for bulk geochemistry using an ITRAX x-ray fluorescence (XRF) core scanner with a molybdenum tube running at 30kV and 55mA with ten-second exposure times (Croudace et al., 2006). The ITRAX provides an image, an x-radiograph showing relative density, and results for the relative abundances of a variety of elements. Along the Hudson River, introduction of metals to the sediments has been particularly useful as a relative dating technique marking the onset of the industrial era (1850 C.E.) (e.g. Williams et al., 1978; Benoit et al., 1999; Kemp et al., 2017). Thus, particular attention was paid to patterns in the relative abundance of heavy metals including lead (Pb) and zinc (Zn). In addition, zirconium (Zr) is used as a proxy for grain size, and relative decreases in potassium (K) have been used to mark peat development (Croudace and Rothwell, 2015), and were employed in this study to identify the onset of marsh development and changes in inorganic sediment supply.

2.4.4 *Sediment physical characteristics*

Following non-destructive ITRAX scanning, cores were subsampled at 10cm intervals, as well as above and below identified lithologic transitions for loss on ignition (LOI). When possible, samples of uniform volumes (1 cc) were taken with modified syringes. Some samples were too fibrous or too unconsolidated for the uniform volume method to be to be possible, so bulk samples of 2-3 cm^3 were taken. All subsamples were placed into crucibles wet, then dried at 100°C, then burned at 550°C for 4 hours and weighed after each step to measure water content and percent organic (Heiri et al., 2001). After LOI, samples were gently disaggregated with mortar and pestle then run through a Beckman Coulter LS 13 320 laser diffraction particle size analyzer with a range of 0.4 µm to 2000 µm, 15 seconds of sonication before running the sample, and a run time of 60 seconds. An alternative digestion method using a double treatment of 30% hydrogen peroxide was also tested (Yellen et al., 2016). However, following this digestion method lignin-rich organic material was still evident upon inspection with a 100x microscope, resulting in anomalously coarse grain size distributions when compared to grain sizes obtained at the same sampling depth following LOI treatment.

Based on LOI results, we also calculated an average dry bulk density for each marsh (Equation 1) using the mass and volume of the wet sample to calculate this (Equation 2). We calculated this using percent water, organics, and clastics from the LOI data, assuming samples were 100% saturated when weighing them wet. For the samples where we were unable to get a uniform volume sample, we calculated approximate sample volumes assuming an organic density of 2 g/cm^3, water density of 1 g/cm^3, and clastic sediment density of 2.65 g/cm^3 (Equation 2). We checked this method by doing this calculation for the samples of known volume.

Calculating the dry bulk density allows us to estimate the mass of clastic sediment in the entire marsh, and therefore how many metric tons per year are accumulating at each location. To do these calculations, we estimate the area of each marsh using Google Earth. These estimates include open water within the marsh, and therefore provide an upper bound of marsh area and sediment mass accumulation. The area of each marsh, average accumulation rate since the onset of ^{137}Cs, and the dry bulk density provide us with an upper bound estimate of how much sediment is being trapped in each site (Table 5). For these calculations, the average accumulation rates and percent clastic since 1954 are used to compare to modern estimates of annual Hudson River sediment yield (0.4 Mt) (Woodruff et al., 2001).

$$\underline{\textit{Equation 1:}}\quad \rho_{drybulk} = ((1 - porosity) * \rho_{wetbulk}) * 1000$$

$$\underline{\textit{Equation 2:}}\quad \rho_{wetbulk} = \frac{Mass_{sample(wet)}}{V_{sample(wet)}}$$

$$\underline{\textit{Equation 3:}}\ V_{sample} = \frac{Mass_{Organics}}{Density_{Organics}} + \frac{Mass_{Water}}{Density_{Water}} + \frac{Mass_{Sediment}}{Density_{Sediment}}$$

2.4.5 *Age constraints on sedimentation*

A combination of techniques were used for determining age constraints including gamma spectroscopy, XRF heavy metals, and historical charts. At least one core at each location was selected for depth profiles of ^{137}Cs to determine ages of modern sediments. The onset of ^{137}Cs in 1954 and peak in 1963 is associated with atmospheric testing of nuclear bombs and gives us two modern age constraints to use for calculating accretion rates (Pennington et al., 1973). Subsamples at varying depths were dried at 100°C, ground into a powder, and analyzed using a Canberra GL2020R low-energy germanium detector (Pennington et al., 1973) for both the measurements of ^{137}Cs and unsupported ^{210}Pb activities. The onset of heavy metals (Zn and Pb) from XRF data were also employed as an age horizon associated with the 1850-1900 onset of industrialization (e.g. Williams et al., 1978). Historical maps and aerial photos were also used for constraining approximate dates of anthropogenic impacts and construction in the area around each location. Average accumulation rates and associated age models are based on the gamma spectroscopy measurements of ^{137}Cs and ^{210}Pb in addition to the onset of heavy metals.

2.5 Results and Interpretations

The various elements from XRF data presented can be suggestive of environmental changes, anthropogenic pollution (increasing Zn), peat development (decreasing K), and maturity and grain size of sediments (increasing Zr) (e.g. Croudace and Rothwell, 2015; Koinig et al., 2003). The LOI data gives us the percentage of organics, which is useful in identifying the onset of a marsh environment with a high organic to clastic ratio. The grain size data is indicative of depositional environment, with larger grain sizes indicating high energy fluvial systems and small grain sizes suggesting low-energy systems like marshes and mudflats. Presented here are core transects for each marsh showing x-radiographs, elemental XRF Zinc (Zn) data, LOI results, and grain size. Additionally, for each location, one core is shown in more detail with an graphic stratigraphy column and additional elemental XRF results (Zr and K). The horizontal grey line on these figures depicts the change in deposition due to the emplacement of the anthropogenic shoreline modification at each site and is placed where the grain size change is most significant. Results for the Tivoli Bays are split into two sections, as one is a mature marsh (TVN) and the other remains a tidal mudflat (TVS).

2.5.1 *Stockport Marsh (SPM)*

Across this marsh we collected cores from five sites as a transect from north to south away from the dredge spoils and will display results from the three representative primary cores SPM1, 4 and 7 in this section. SPM1 shows a steady increase in Zn from the base of the core at 1.5 m with a corresponding increase in LOI up-core (Figure 10). SPM4 and SPM7 show increasing Zn at shallower depths, closer to 0.7 m, and a subsequent up-core decrease beginning near 0.3-0.4 m. The coincident increase in LOI with the increasing Zn across all three cores is indicative of the beginning of marsh development. The rise in Zn is indicative of a change in depositional setting linked to fine-grained sediment, which trap metals more effectively than coarse-grained sediments (Singh et al., 1999).

Overall, the sediment in all three cores have a median grain size, D50, under 50µm, with deviations above this range in the lower parts of the core. SPM1 and SPM4 show increasing grain size down-core (near 1.2 and 1.1 m, respectively). Based on historical charts and topographic maps, dredge spoils to the north of the marsh were placed there near 1930 (Figure 7). The ^{137}Cs results give variable accumulation rates from SPM1 to SPM4, supported by the depth differences for the increase in Zn. SPM1 has a very high accumulation rate, between 1-2 cm/year, while SPM4 is lower at approximately 0.9 cm/year (Table 4). Using the various age constraints for SPM1, the average accumulation rate is 1.18 cm/year (Figure 16). This rate is much faster than annual sea level rise at 0.54 ± 0.14 cm/year in Albany (Ralston et al., 2018). Based on the deposition rate and the average depth of the cores, the sediment being stored in the Stockport Marsh is approximately 1000 tons/year, just 0.25% of the Hudson River annual sediment load (Table 5).

2.5.2 *Tivoli North (TVN)*

At Tivoli North (TVN) we recovered cores from five sites along a transect from the outlet of Stoney Creek to the railroad trestle (Figure 8). Across the TVN transect, the increasing Zn signature was not clearly evident and thus is not shown so that changes in LOI and grain size can be seen (Figure 11). LOI results increase at 1.5 m from near 0% to almost 50% in TVN2, TVN3, TVN1, and TVN4, concurrent with decreasing grain size up-core. TVN5 is the most landward core and shows the most moderate increase in LOI up-core.

In TVN3 there is a rapid decline at 1.1 m in the relative abundance of K (Figure 11). Decreasing K is indicative of peat development, so this change likely marks the transition to a full marsh environment with peat building up (Croudace and Rothwell, 2015). Elemental Zr shows a steady decline from 2.0-1.4m followed by a sharp decrease at 1.4 m, which is indicative of the decreasing grain size and maturity of the sediments coming into the system because it is highly resistant to weathering (Koinig et al., 2003; Yellen et al., 2014). Age constraints for the TVN3 core show the onset and peak in ^{137}Cs at 0.65 and 0.35 m, respectively, with an average accumulation rate of 0.83 cm/year (Figure 17). Based on the deposition rate and the average depth of the cores, the sediment being stored in the Tivoli North marsh is approximately 1800 tons/year, 0.45% of the annual budget of the Hudson River (Table 5).

2.5.3 *Tivoli South (TVS)*

Tivoli South Bay was the only site that produced high-quality GPR results (Figure 12). The topmost unit is shallower toward the east but moving westward it extends about a meter down from the surface-water interface. This unit aligns with the changes in the profiles of Zn, LOI, and grain size across the transect, with TVN3 to the east being the shallowest transition to marsh sediments. A second unit beginning at 1 m below the interface and deepening to 5 m to the west encompasses the lower portion of all three cores collected. None of the cores extend down into the third stratigraphic unit visible in the GPR profile.

Three cores were collected from the mudflats of the Tivoli South embayment along a west-to east transect (Figure 8). The transect begins 120 m east of the railroad causeway on the Hudson River side of the bay (TVS1) and ends at TVS3 located 200 m west of the mouth of the Sawkill Creek, a side tributary that enters directly into the bay. The XRF results for TVS1 and TVS2 show an initial increase in Zn at a sediment depth of 1.3 m, shallowing to a depth of 0.5 m for TVS3 which is nearest the outlet of the creek (Figure 10). Across all three cores, the increase in Zn in coincident with rising LOI and decreasing grain size. Below this Zn onset LOI is low and relatively constant, with values ranging from 2-3% in TVS1 below 1.3 m (Figure 13). LOI steadily increase above the 1.3m transition to roughly 6% LOI at a depth of 0.9 m and above. Above 1.3 m in TVS1, there is also a steady decline in the abundance of K concurrent with the observed increase in Zn. The Zr profile shows a sharp decrease above 1.3 m, matched by the increase in LOI and decrease in grain size (Figure 13). The onset and peak of ^{137}Cs in TVS1 appear at 0.4 and 0.35 m, respectively, both resulting in an accumulation rate of 0.72 cm/year (Figure 18). Based on the accumulation rate the sediment being stored in the Tivoli South mudflat is approximately 2900 tons/year (Table 5) amounting to 0.74% of the long-term annual sediment budget in the Hudson River.

2.5.4 *Esopus Marsh (ESP)*

600 m long jetties extend from the mouth of the Esopus Creek into the Hudson River with a maintained navigation channel in between and fringing marshes on the north and south sides (Figure 8). Five marsh cores were collected from this site and include one on the north side of the jetties and four on the south side. The four cores collected from the south side show variable depths for the onset of industrial Zn at depths of: 0.9 m in ESP3, 0.7 m in ESP2, 1.2 m in ESP4 (Figure 14). Similar to the TVN and SPM results, this rise in Zn is also accompanied by an increase in organics and drop in grain size. The ESP3 core shows the onset and peak of ^{137}Cs at 0.65 and 0.5 m respectively at an accretion rate of 0.66 cm per year (Figure 19). Based on the deposition rate and the average depth of all the ESP cores, the sediment being stored in the southern Esopus marsh is approximately 1800

tons/year which is just 0.46% of the long-term annual sediment flux of the Hudson River (Table 5).

ESP5, separated from the other cores at ESP on the northern side of the jetties, shows evidence of long predating the industrial era. However, lacking radiocarbon dates and a comprehensive age model, we cannot be certain of the age of the northern marsh at Esopus. This site is proximal to a very sediment-rich catchment delta where the Esopus creek enters the Hudson River (Ralston et al., 2013; Yellen and Steinschneider, 2019). Down-core in ESP5 there are several variations in LOI that are less evident in the XRF data and grain size (see Appendix: Figure 22). The onset and peak of ^{137}Cs at ESP5 occur at 1.0 and 0.8 m, respectively, requiring an accumulation rate of 1.11 cm/yr since 1954 (Figure 20). However, LOI, grain size, and depth of the core indicate that the northern side of the marsh likely existed prior to the modern industrial era. The results from the ESP5 core are indicative of a complex depositional history, likely due to its location near the delta of a sediment rich river.

2.5.5 *Iona Island (INA)*

Seven cores were collected from Iona Marsh all on the western inland side of the railroad causeway that runs along the west bank of the Hudson River (Figure 9). INA4, INA3, INA2, and INA7 represent a south-to-north transect through the marsh, while INA4, INA1 and INA5 lie along an east-to-west transect. The remaining INA6 core is located in between the north-to-south and east-to-west transects and is closest to the location of the previously derived millennial-scale reconstruction of marsh accumulation for the site by Chou (2010). At Iona the onset of industrial Zn begins at a depth of approximately 0.4 m in both INA2, 3, and 4 (Figure 15). The LOI results for INA5 show wide variability and a slow decline in the surface 0.2 m but remain relatively stable around an average of 40%. The grain size results are relatively constant through INA2 and 5, while INA4 and 3 each show increasing D50 values from 0.6-0.2 m and a subsequent decrease in the surface 0.2 m. The longest core collected from Iona Marsh, INA5, had an onset and peak of ^{137}Cs at 0.15 and 0.025 m, and when combined with other age constraints results in an accumulation rate of 0.08 cm per year (Figure 21). This low accumulation rate suggests that marsh development was prior to the construction of the railroad causeway in 1851, consistent with previous results from Chou (2010). Based on the deposition rate and the average depth of the cores, the sediment being stored in the Iona Island marsh is approximately 30 tons/year (Table 5), about 0.01% of the Hudson River Estuary annual budget.

2.6 Discussion

Study sites near anthropogenic features like dredge spoils, railroad causeways, and jetties exhibit sediment accretion rates that exceed modern and projected rates of sea level rise. Our results show that some of the marsh systems on the Hudson River have developed rapidly in response to the creation of sheltered conditions that have allowed for fine-grained material to accumulate. Thus, marsh initiation and growth in this environment seems to be governed by suitable hydrodynamic conditions and not by sediment supply. It is estimated that between 0.4 to 1.0 Mt is delivered to the Hudson River Estuary annually, with most of that getting trapped in the estuary and only exiting the system during extreme flooding events (Woodruff et al., 2001; Ralston et al., 2013). For the purposes of this study, we used the lower estimate of Hudson River sediment flux (0.4 Mt) to calculate upper bound estimates of annual trapping at our marsh locations, between 0.01-0.74% of the river’s sediment budget (Table 5). Woodruff et. al. (2001) and Wall et. al. (2008) suggest that there are isolated pockets of anomalously high deposition in the Lower Hudson River Estuary, and results from this study indicate that one such environment is likely the anthropogenic embayments along the Hudson River banks, similar to results from a study on the Connecticut River wetlands (Woodruff et al., 2013b).

The impact of past and future climate change is an important factor in the stability of these marsh systems, particularly with respect to rising sea levels. The mean water level has risen approximately 0.54 ± 0.14 cm/year at Albany, NY and 0.33 ± 0.07 cm/year at The Battery, NY since 1965 (Ralston et al., 2018) and results from this study indicate that the rising water levels encourage high deposition rates. Additionally, modeling results from Tabak et. al. (2016) show a net increase in tidal wetland extent in the Hudson River in almost all sea level rise scenarios in response to the development of more sheltered off-river environments. Results from this study and others in the region indicate that the tidal range, mean water level, and sediment storage along the Hudson River have changed in response to the anthropogenic modifications to the system in the last few hundred years.

2.6.1 *Post-industrial Marshes: Stockport, Tivoli Bays, Esopus*

Based on prior studies we would expect low sediment yields across the Hudson River watershed due to the frequent construction of dams over the past few centuries (Fox et al., 2016; Peteet et al., 2018), however this constraint on sediment does not seem to be hindering the growth and accumulation of marshes along most of the Hudson River. Throughout the Hudson River watershed, dam trapping efficiency is very low relative to the total annual sediment budget of the Hudson River. For example, all of the sediment trapped by dams in the Stockport Marsh watershed accounts for only 20-30% of the annual sediment budget of the Hudson River (Brian Yellen, personal communication).

One of our primary age constraints is the increase in heavy metals, indicative of rising pollution during the industrial era between 1850 and 1900, as well as the enhanced trapping of fine-grained, organic material with a high affinity for heavy metal adsorption (Singh et al., 1999) behind sheltered man-made landforms such as railroad causeways (TVN and TVS), dredge spoil islands (SPM), and jetties (ESP). Previous studies of Tivoli North and Iona marshes used radiocarbon dates to assess ages of the marshes. Sritrairat et. al. (2012) dates marsh material back to 1100 years before present at a point behind the tombolo between Tivoli North and South Bays, indicating that this naturally sheltered region has supported marsh growth for a substantially longer period of time than within the embayment defined by the railroad causeway. Based on the historical chart depths of the embayments as a whole, Tivoli South began as a deeper lagoon than Tivoli North (Figure 8). At the outlet of adjacent watersheds of similar size, and with comparable sediment accumulation rates within these basins, it appears that the available accommodation space played an important role in the current state of each embayment as a marsh (TVN) and mudflat (TVS). The difference between these bays does not appear to be due to enhanced trapping and more organic production in TVN, but rather that TVS was deeper than TVN following railroad constructions and in turn has taken longer to infill and transition to a marsh environment.

2.6.2 *Pre-Industrial Marsh: Iona*

Based on the radiocarbon dates for the Iona Marsh core analyzed by Chou (2010), the marsh formed at approximately 4300 years CE. The Chou (2010) core was collected much closer to the road and bedrock islands, however, and has much higher deposition rates than in the INA cores analyzed in this study (approximately 0.78cm/yr since 1963). Based on results from this study the annual mass of sediment accumulated (400 t per year), less than 0.1% of the annual sediment budget of the Hudson River, is the smallest of all sites analyzed. This example indicates that not all marshes located behind anthropogenic structures are as recent as those structures. At Iona marsh, the sheltered region around the bedrock islands has supported marsh growth for several millennia prior to railroad construction. The example from this site illustrates that older systems that have reached equilibrium need less sediment to keep pace with sea level rise.

2.7 Conclusion

The study of anthropogenic marshes in the freshwater tidal portion of the Hudson River suggests that there is no shortage of sediment supply along the Hudson River, only a shortage of accommodation space. Our results from four anthropogenic embayments in the freshwater tidal portion of the Hudson River show sediment accumulation rates between 0.6-1.1 cm per year since 1963 which far outpace sea level rise (Table 4). Our results suggest that man-made landforms such as railroad causeways, dredge spoil islands, and jetties had the unintended consequence of establishing low-energy embayments along the sides of the Hudson River. These sheltered environments in combination with a steady supply of sediment from the tidal Hudson River supported relatively high sedimentation rates and the rapid development of freshwater tidal marshes (in the span of 50-150 years). Future research to continue assessing sediment transport along the tidal Hudson River and primary sediment storage locations would be invaluable for informing future marsh and wetland management decisions. These accidental historical successes of anthropogenic marsh creation provide an opportunity to identify the physical conditions required to successfully support wetland development and case studies for the development of wetland management plans.

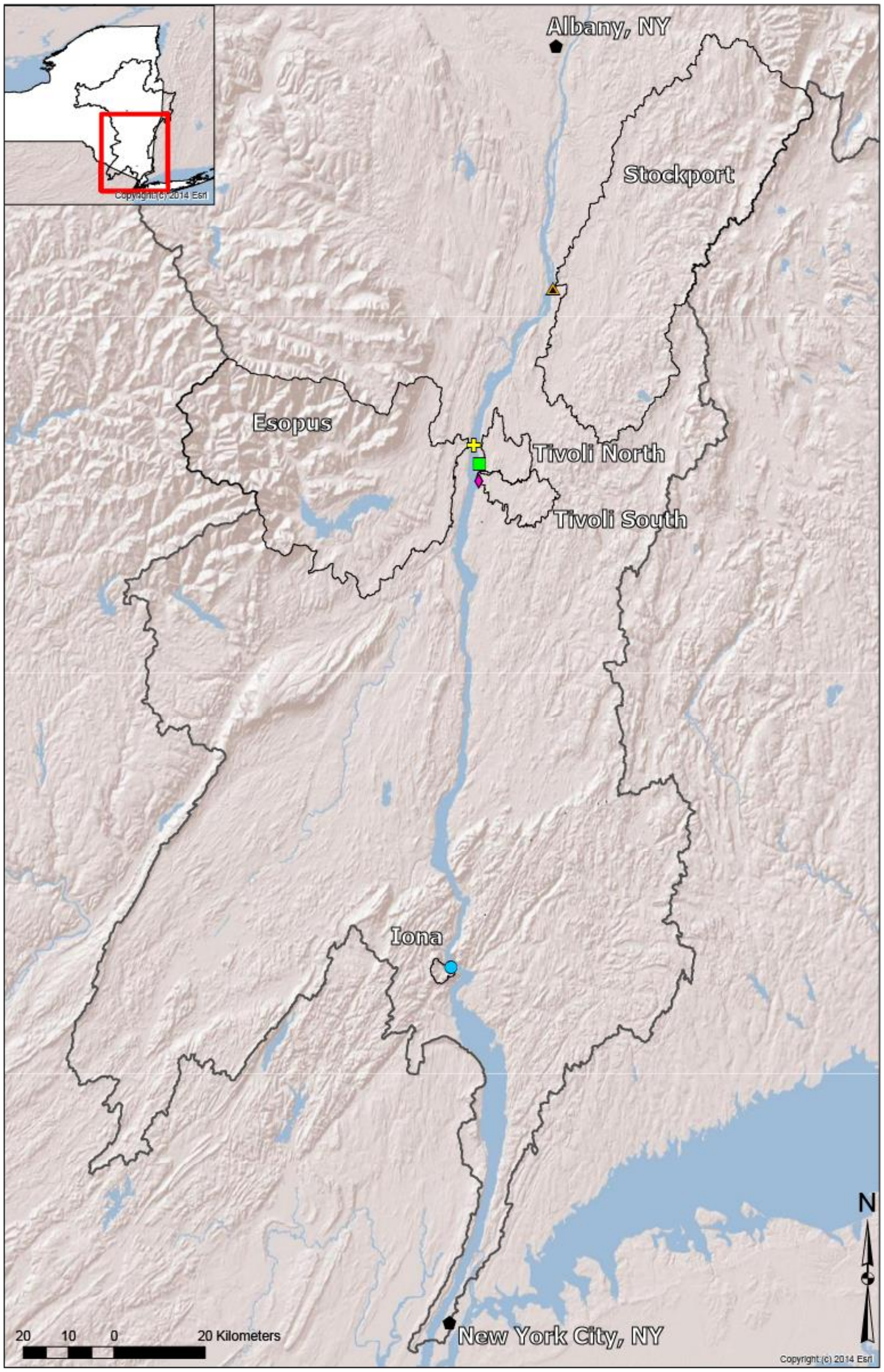

Figure 6 Map of the entire tidal portion of the Hudson River from The Battery north to Albany, NY. The catchment is outlined in black for each marsh and the entire Hudson River basin at large (see inset). Each marsh at the outlet of these catchments is marked by a different colored symbol: an orange triangle for Stockport Marsh, a green square for Tivoli North, a pink diamonds for Tivoli South, a yellow plus sign for Esopus Marsh, and a blue circle for Iona Island.

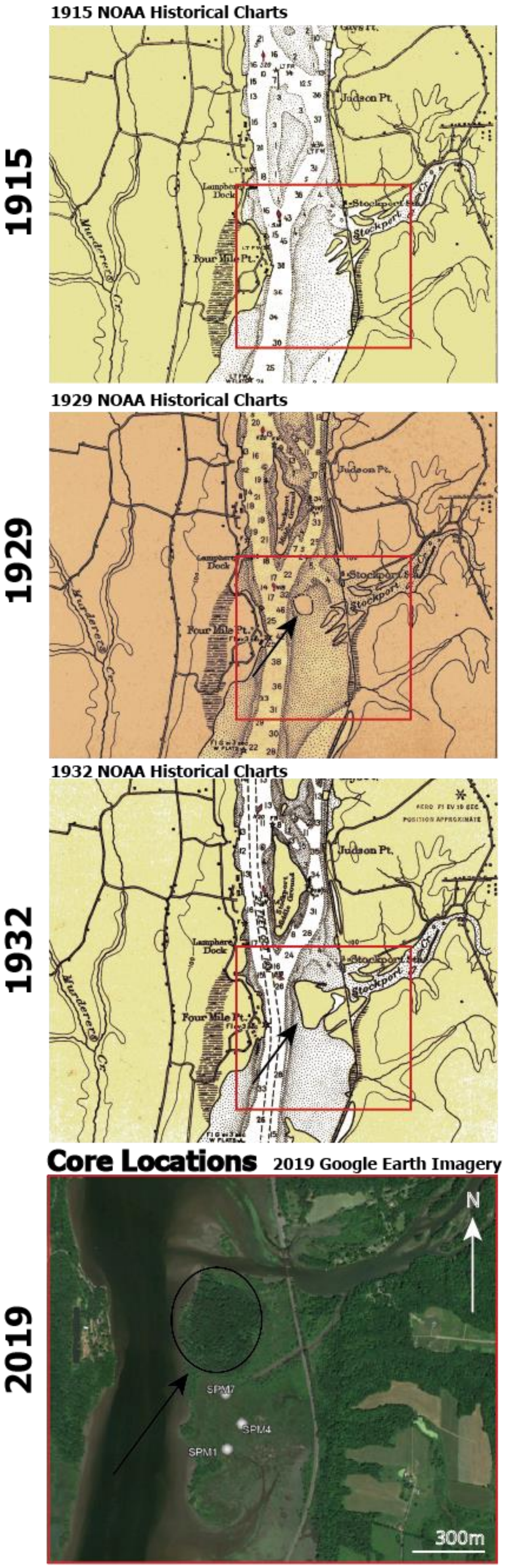

1915 NOAA Historical Charts

1929 NOAA Historical Charts

1932 NOAA Historical Charts

Core Locations 2019 Google Earth Imagery

Figure 7 Stockport marsh historical charts from 1915, 1929, and 1932 showing the emplacement of dredge spoils and marsh development since then. The red box in the three charts outlines the location of the satellite image at the bottom, showing core locations. The black arrow in the lowest three images highlights the location of emplaced dredge spoils at the mouth of the river in the 1920s and 1930s.
Water depths shown are in feet below mean low water. All historical chart images are from NOAA's Office of Coast Survey Historical Map & Chart Collection (https://historicalcharts.noaa.gov).

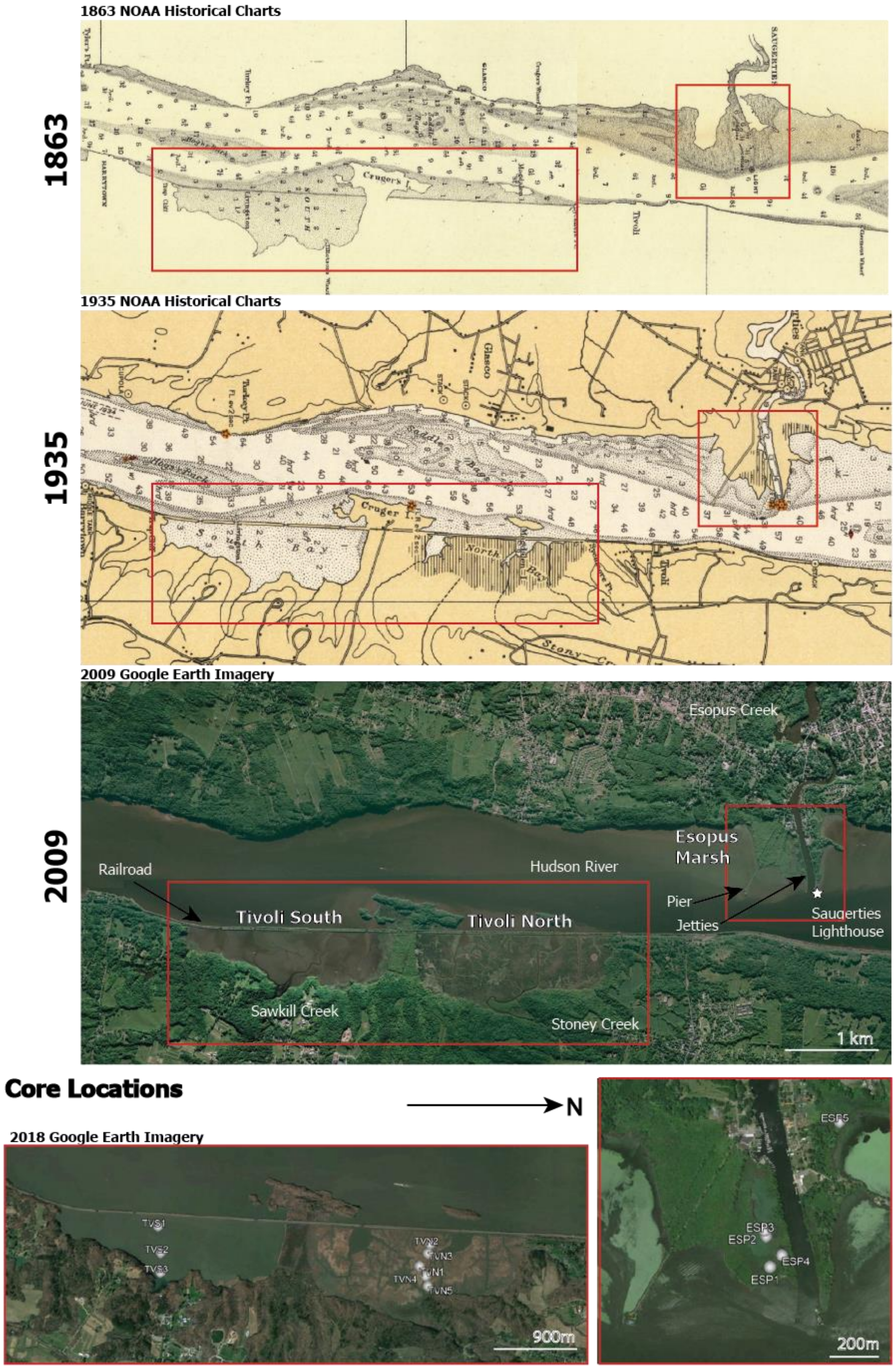

Figure 8 The stretch of the Hidson River from Esopus to the Tivoli Bays showing historical images from 1863 and 1935, and satellite images from 2009 and 2016. The historical charts illustrate the construction of piers at Esopus and marsh development at Esopus and Tivoli Bays. The red box in the three images outlines the location of the satellite images at the bottom, showing core locations in the Tivoli Bays and Esopus marsh. Water depths shown are in feet below mean low water. All historical chart images are from NOAA's Office of Coast Survey Historical Map & Chart Collection (https://historicalcharts.noaa.gov).

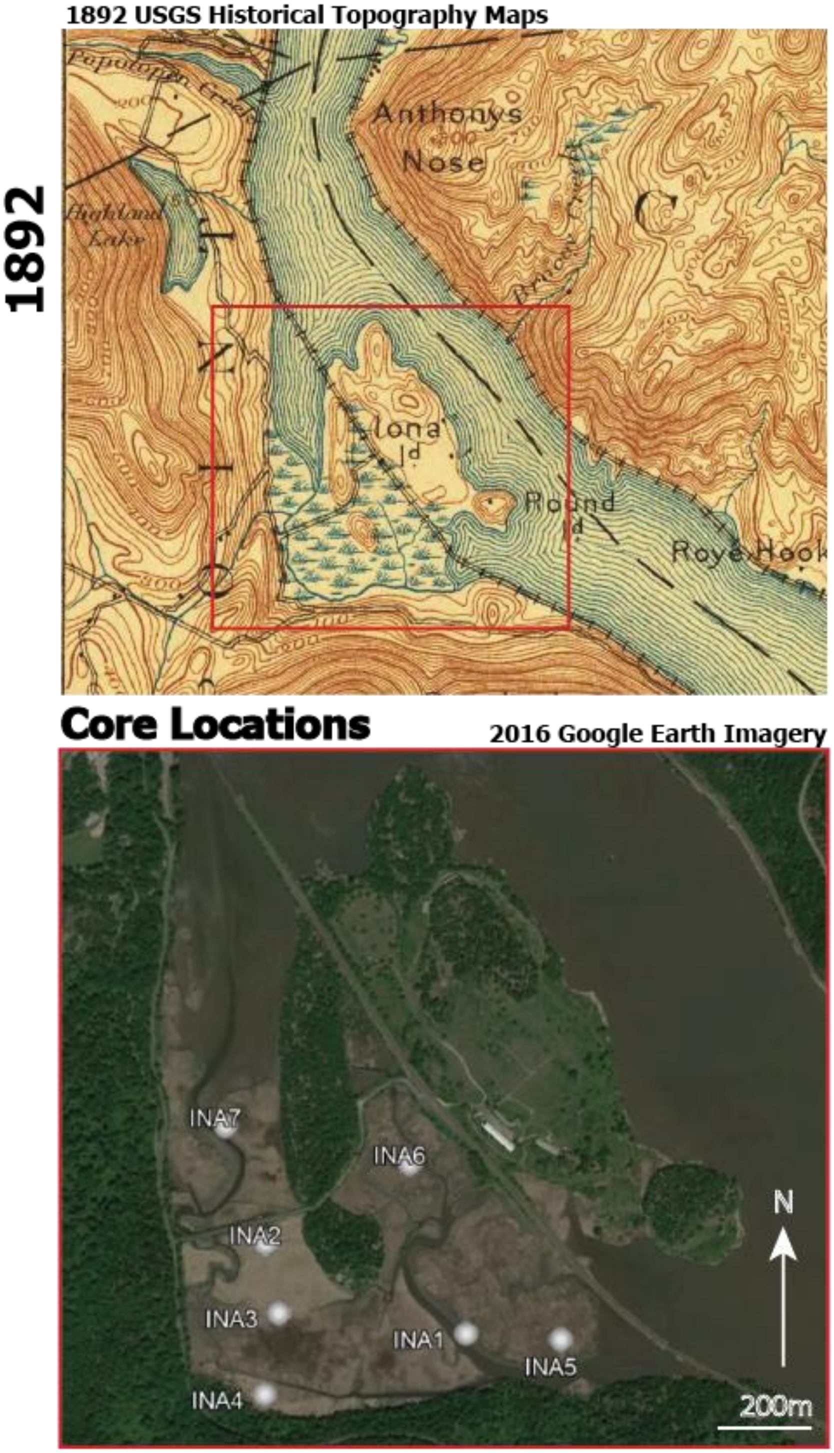

Figure 9 The earliest topographical map of Iona Island from 1892, showing topography of the bedrock islands in the marsh and location of the railroad and causeway through the marsh. The historical map image is from USGS topoView historical topographic maps (https://ngmdb.usgs.gov/topoview/).

Table 3 Summary of details for each location in the study listing catchment area, the month that cores were collected, how many cores were collected, and how deep the longest core was.

Location Name	**Tributary Catchment Area (km^2)**	**Month collected**	**Number of core sites**	**Max. core depth (m)**
Stockport Marsh	1300	06/2017	5	1.5
Tivoli North	60	06/2018	5	3.0
Tivoli South	70	06/2018	3	3.5
Iona Island	10	08/2018	7	3.9
Esopus Marsh	1100	06/2018	5	4.2

Table 4 Age constraints using one core from each marsh site except Stockport, where two cores were measured. For each core, values reported are the depth to the onset (1954) and peak (1963) of 137Cs, and the onset of heavy metals, and the approximate accumulation rates of sediment between these dates. The average accumulation rate are further constrained in the compiled age models (Figures 17-21).

Core	**SPM1**	**SPM4**	**TVN3**	**TVS1**	**INA5**	**ESP5**	**ESP3**
Depth to metals onset (cm)	140	70	150	135	50	150	85
Depth to Cs onset (cm)	110	60	65	40	15	100	65
Depth to Cs Peak (cm)	61	40	35	35	3	80	50
Acc. Rate (cm/yr) metals onset-1954	1.3	0.4	0.8	0.9	0.3	0.8	0.3
Acc. Rate (cm/yr) 1954-2018	1.7	0.9	1.0	0.6	0.2	1.6	1.0

Table 5 Marsh characteristics by site: approximate marsh area, depth to 1954, the average sedimentation rate since 1954, total volume of the sediment, the dry bulk density of sediment at each site, the associated total mass of sediment within each marsh, and mass of sediment deposited annually within each marsh location. All quantities are just for the sediment accumulation since 1954.

Site	**SPM**	**TVN**	**TVS**	**ESP**	**INA**
Marsh Area (km2)	0.19	1.32	0.97	0.25	0.51
Avg. Depth to Cs Onset- 1954 (m)	0.85	0.65	0.40	1.00	0.15
Avg. Sed Rate since 1954 (cm/yr)	1.19	0.83	0.72	0.66	0.08
Total volume of sediment (m3)	161500	858000	388000	250000	76500
Average dry bulk p (kg/m3)	1031	936	1043	908	296
% clastic of bulk density (since 1954)	39	14	47	52	9
Total mass of sediment (metric tons (t))	64938	114780	188196	117132	2128
Mass deposited annually since 1954(t/yr)	1015	1793	2941	1830	33
% of HRE sed budget (0.4Mt)	0.25	0.45	0.74	0.46	0.01

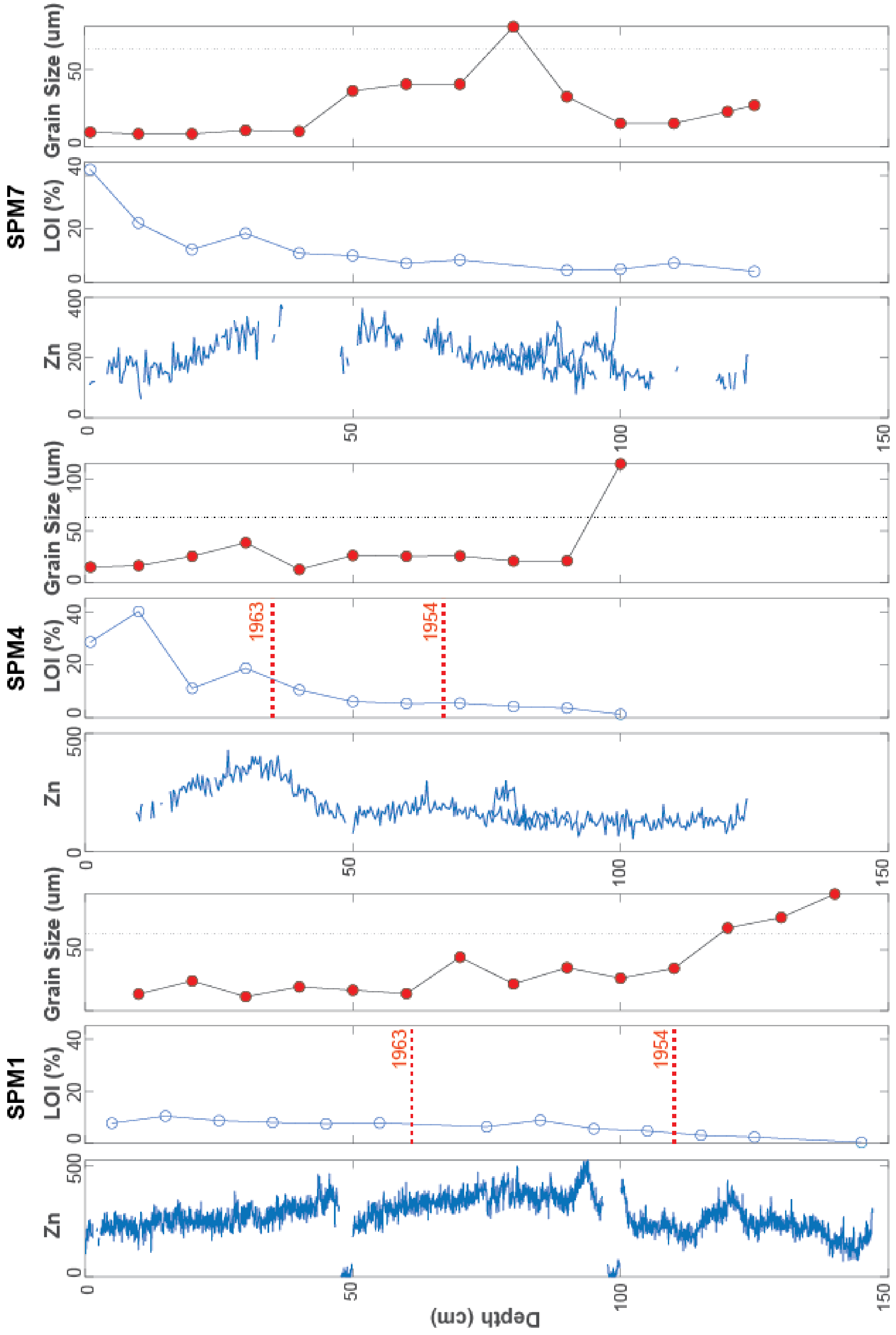
SPM7
Grain Size (um)
0
50
LOI (%)
0
20
40
Zn
0
200
400
SPM4
Grain Size (um)
0
50
100
LOI (%)
0
20
40
1963
1954
Zn
0
500
SPM1
Grain Size (um)
50
LOI (%)
0
20
40
1963
1954
Zn
0
500
0
50
100
150
Depth (cm)

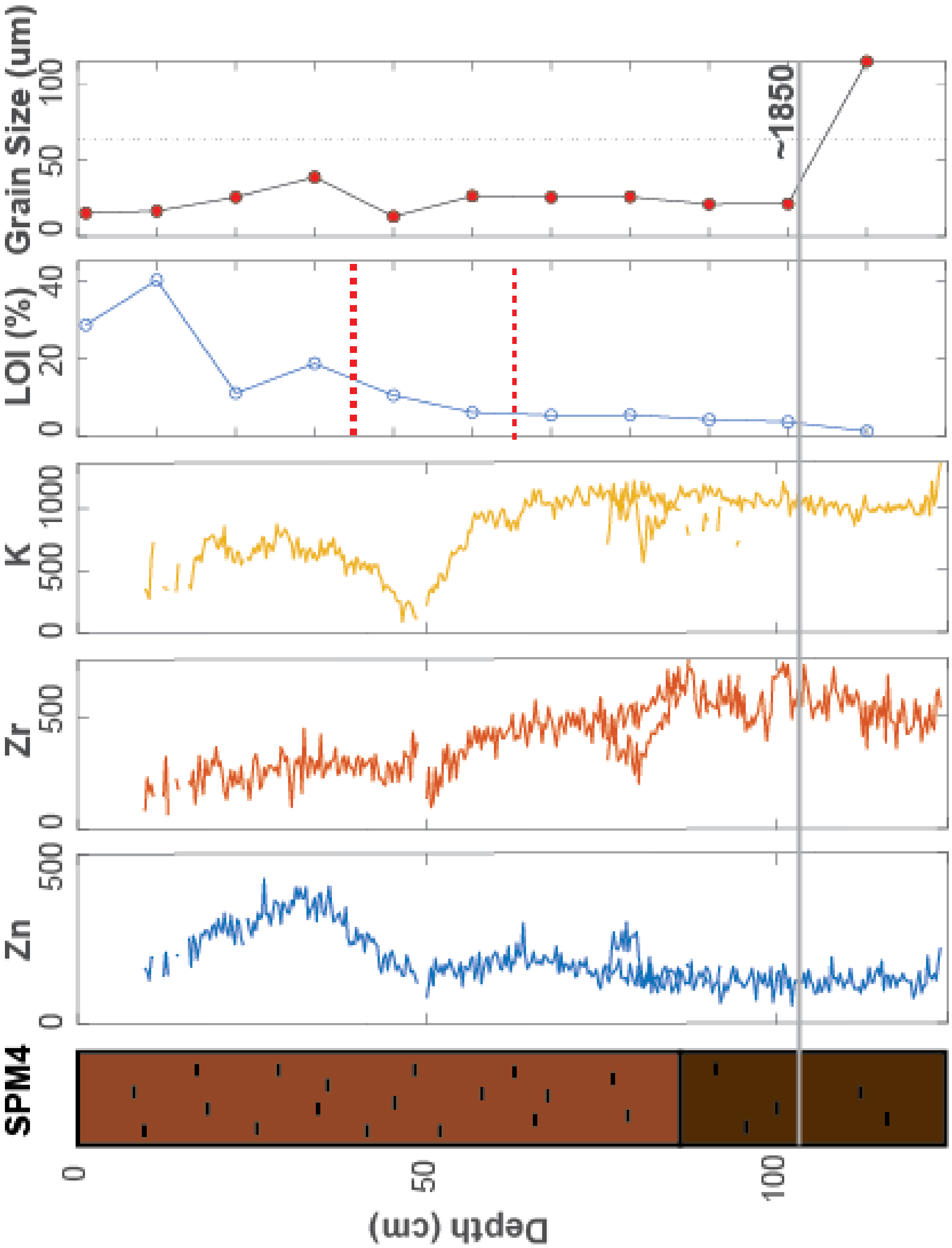

Figure 10 Transect of cores from Stockport Marsh. *Top:* SPM1, 4 and 7 showing Zn XRF data, LOI (%), and grain size (µm) from left to right for each core. *Bottom:* SPM4, the longest core, from left to right showing an lithologic sketch, elemental data of Zn, Zr, K, LOI (%), and grain size (µm). The red dotted lines on the LOI plot mark the onset and peak of ^{137}Cs. The vertical dashed line on the grain size plots is at 63 µm, the distinction between sand and silt. The grey line on the bottom figure marks the change in environment at 1930, placed based on the sharp decrease in grain size.

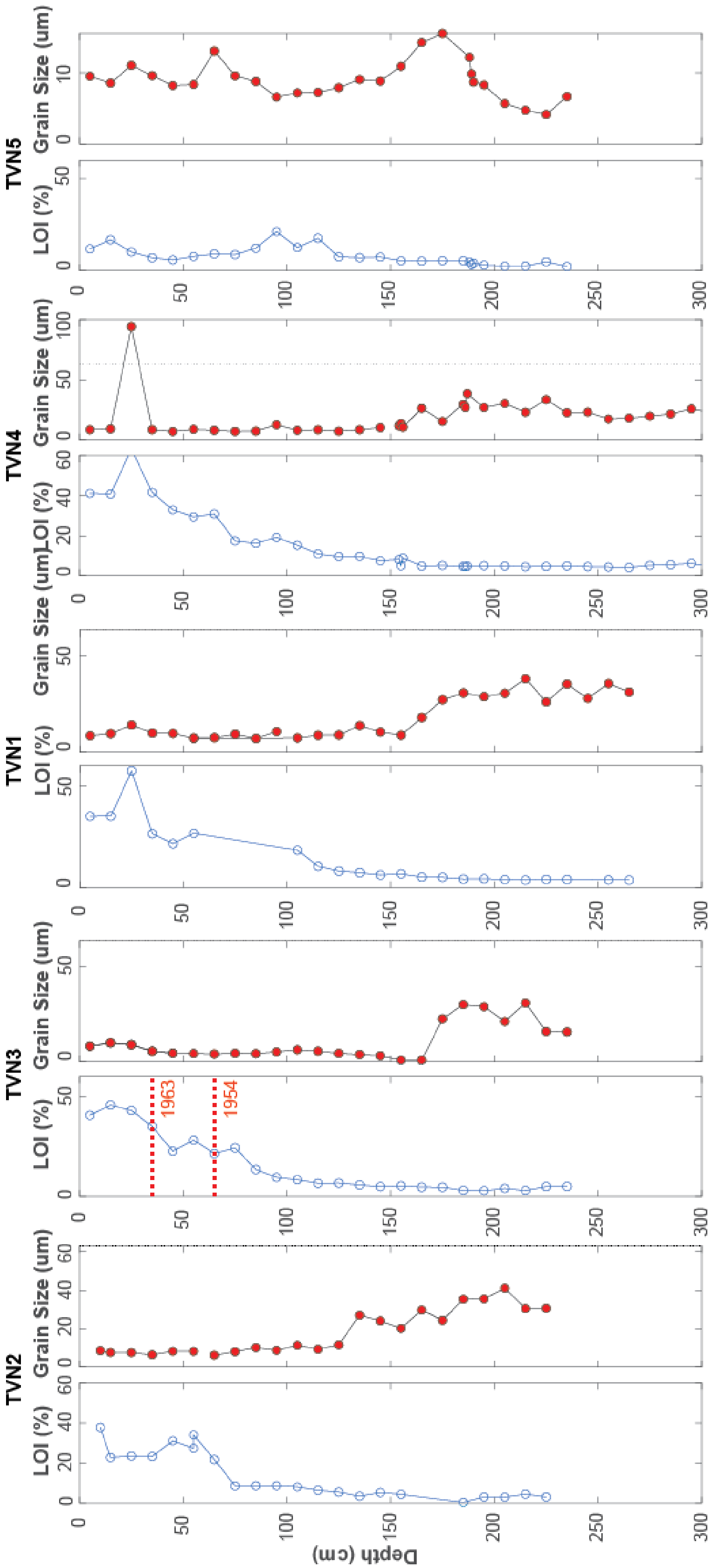
TVN5
TVN4
TVN1
TVN3
TVN2
Grain Size (um)
LOI (%)
1963
1954
Depth (cm)
0
50
100
150
200
250
300

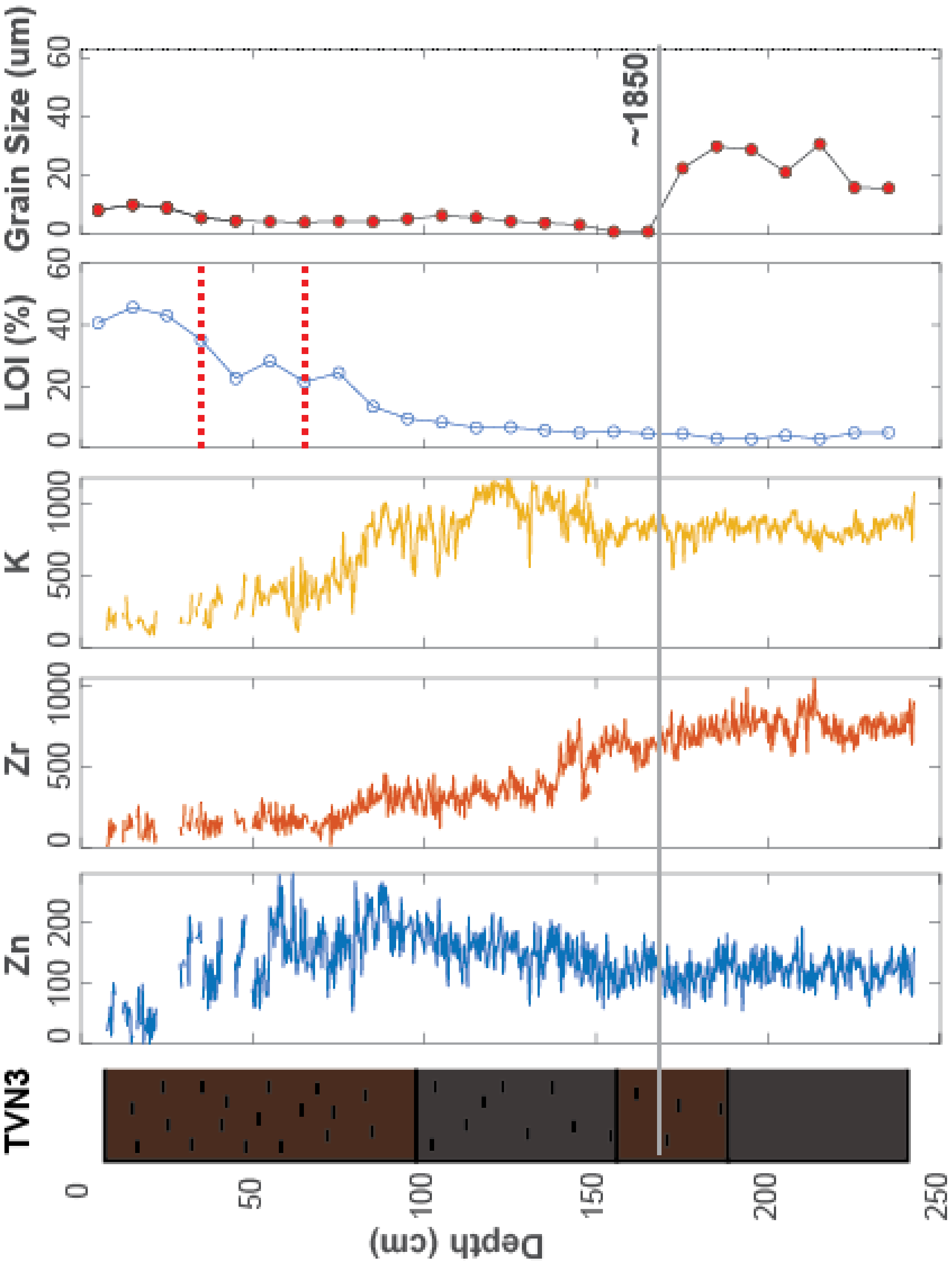

Figure 11 Transect of cores from Tivoli Bay North. *Top:* TVN 2, 3, 1, 4, and 5 showing LOI (%) and grain size (µm) from left to right for each core. *Bottom:* TVN3, the longest core, from left to right showing an lithologic sketch, elemental data of Zn, Zr, K, LOI (%), and grain size (µm). The red dotted lines on the LOI plot mark the onset and peak of ^{137}Cs. The vertical dashed line on the grain size plots is at 63 µm, the distinction between sand and silt. The grey line on the bottom figure marks the change in environment at 1850, placed based on the sharp decrease in grain size.

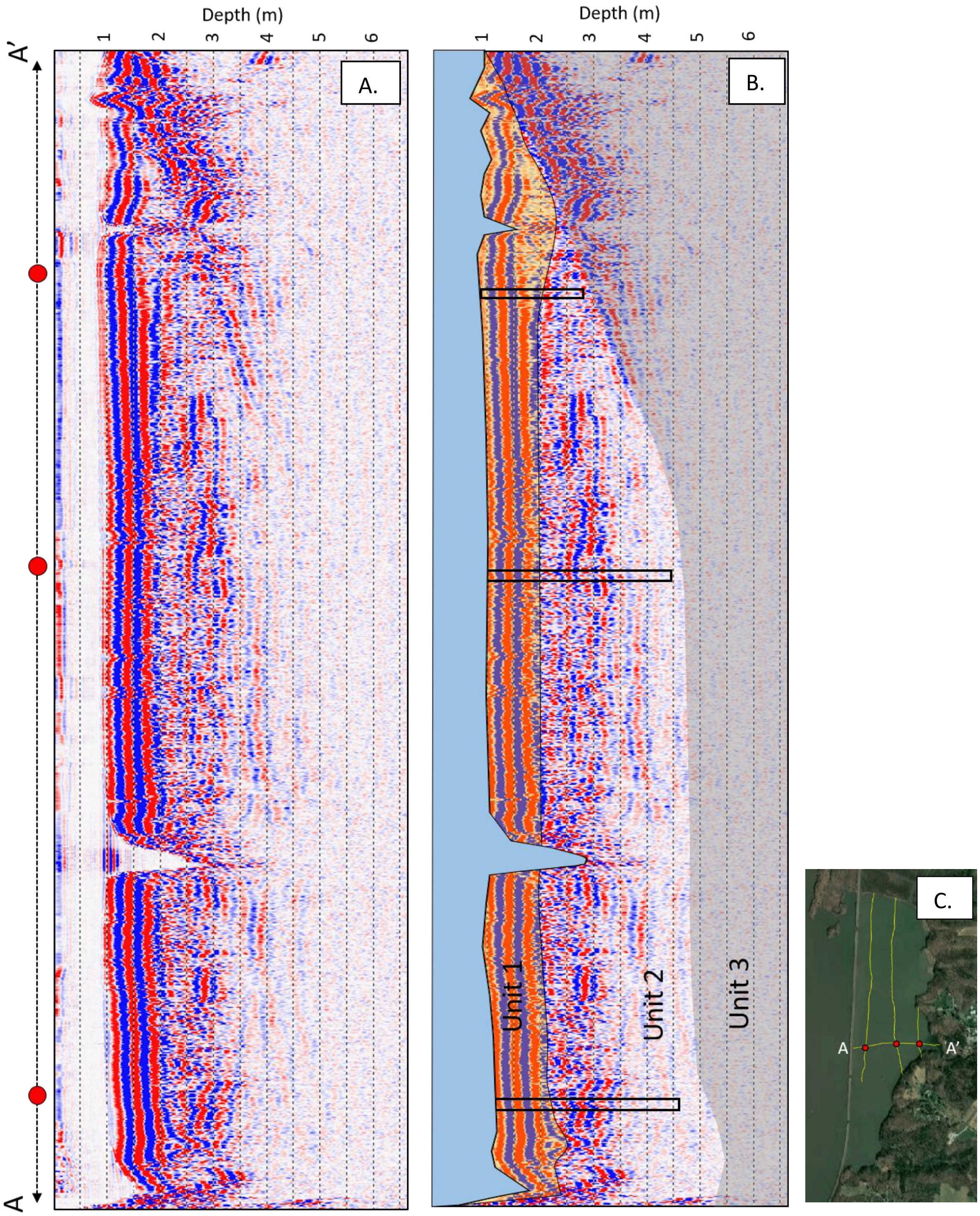

Figure 12 The ground-penetrating radar results from Tivoli South. A) Analyzed results with the different reflectors unaltered. B) The interpreted units from the reflectors, and the core locations across the transect. C) The inset site image shows the location of the A-A’ GPR line.

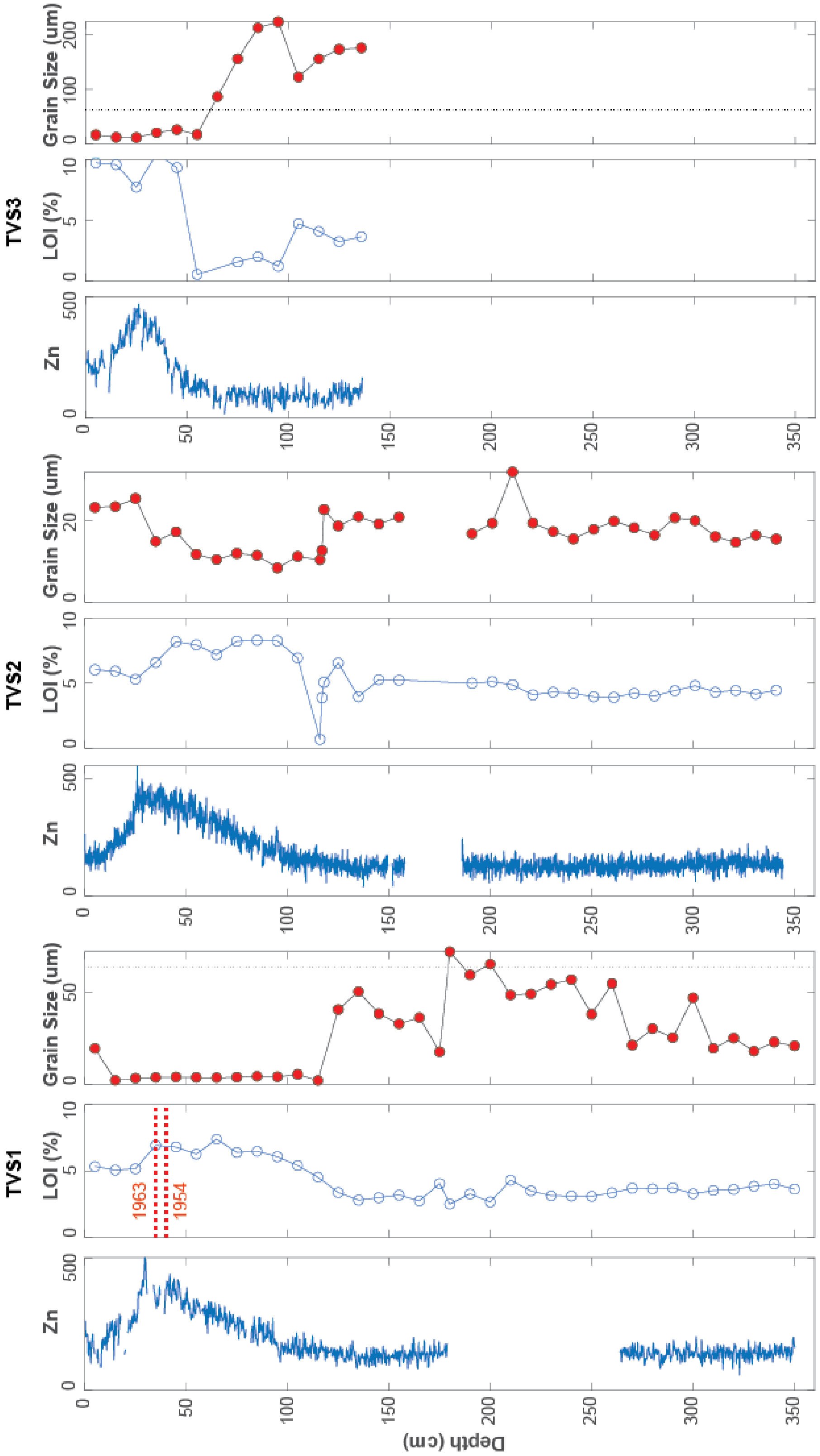
TVS3
Grain Size (um)
0
100
200
LOI (%)
0
5
10
Zn
0
500
0
50
100
150
200
250
300
350
TVS2
Grain Size (um)
0
20
LOI (%)
0
5
10
Zn
0
500
0
50
100
150
200
250
300
350
TVS1
Grain Size (um)
0
50
LOI (%)
0
5
10
1963
1954
Zn
0
500
0
50
100
150
200
250
300
350
Depth (cm)

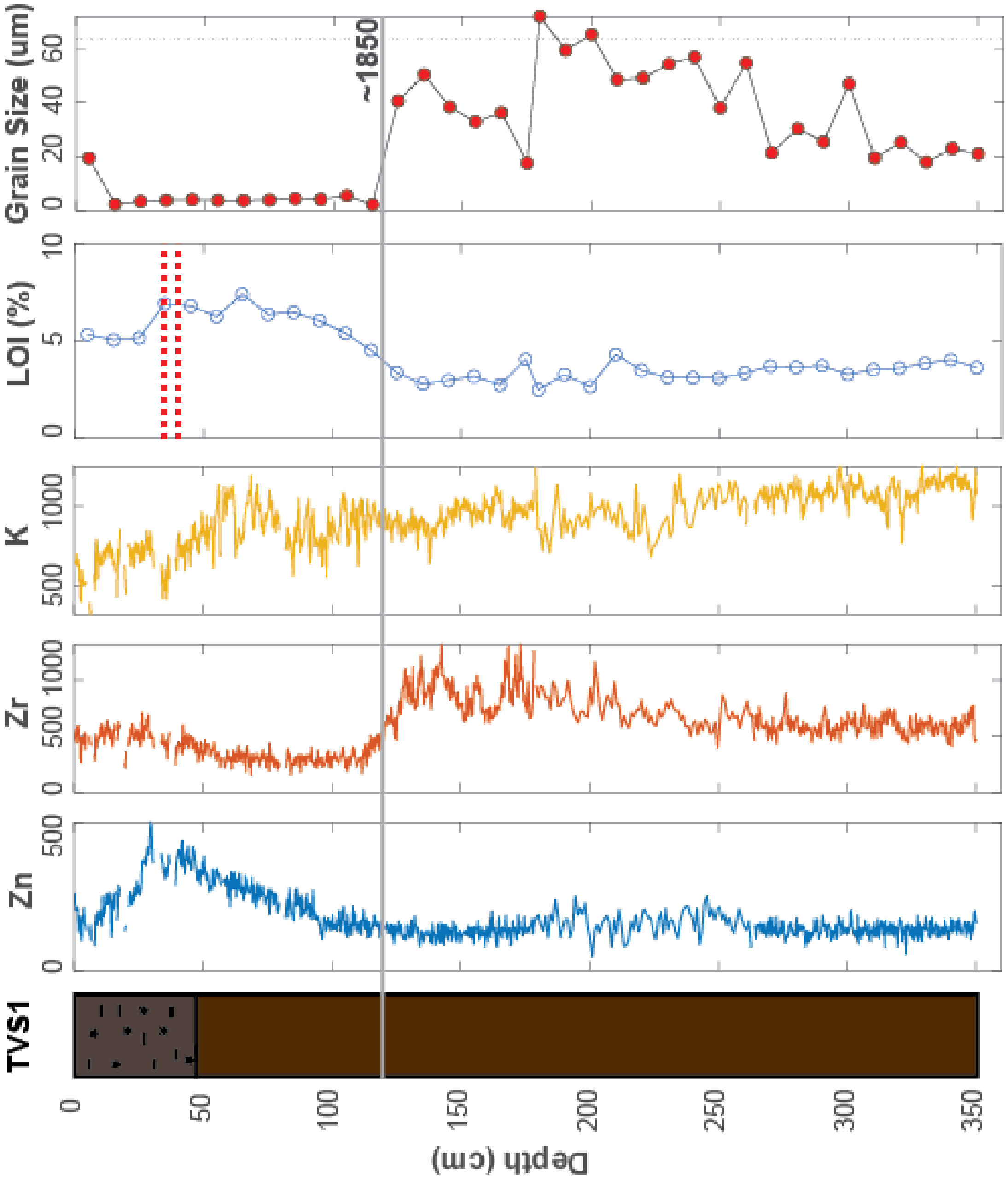

Figure 13 Transect of cores from Tivoli Bay South. *Top:* TVS1, 2, and 3 showing Zn XRF data, LOI (%), and grain size (µm) from left to right for each core. *Bottom:* TVS1, the longest core, from left to right showing an lithologic sketch, elemental data of Zn, Zr, K, LOI (%), and grain size (µm). The red dotted lines on the LOI plot mark the onset and peak of ^{137}Cs. The vertical dashed line on the grain size plots is at 63 µm, the distinction between sand and silt. The grey line on the bottom figure marks the change in environment at 1850, placed based on the sharp decrease in grain size.

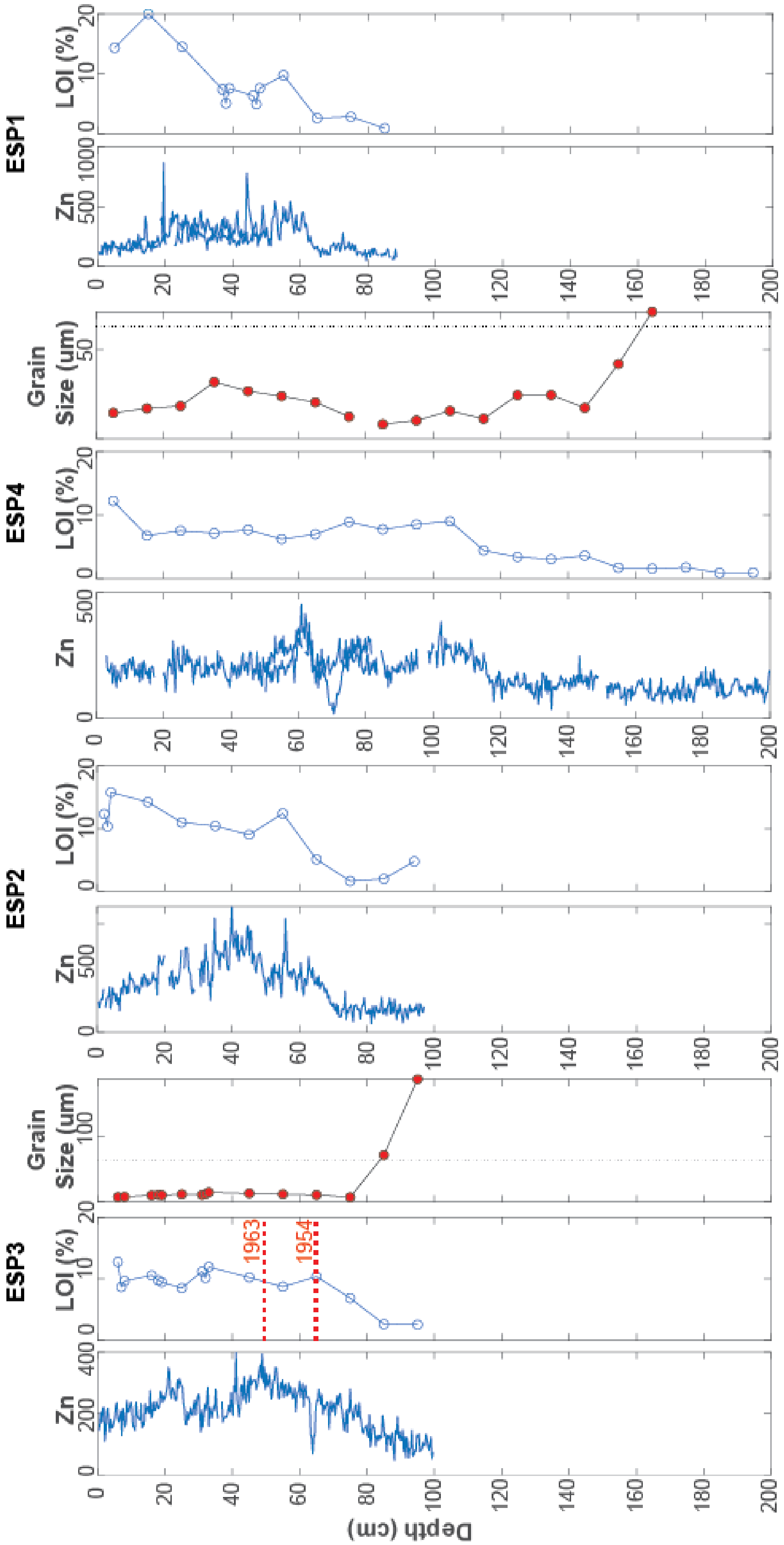
ESP1
ESP4
ESP2
ESP3
Zn
LOI (%)
Grain Size (um)
Depth (cm)
1963
1954
0
20
40
60
80
100
120
140
160
180
200
0
10
20
500
1000
50
100
200
400

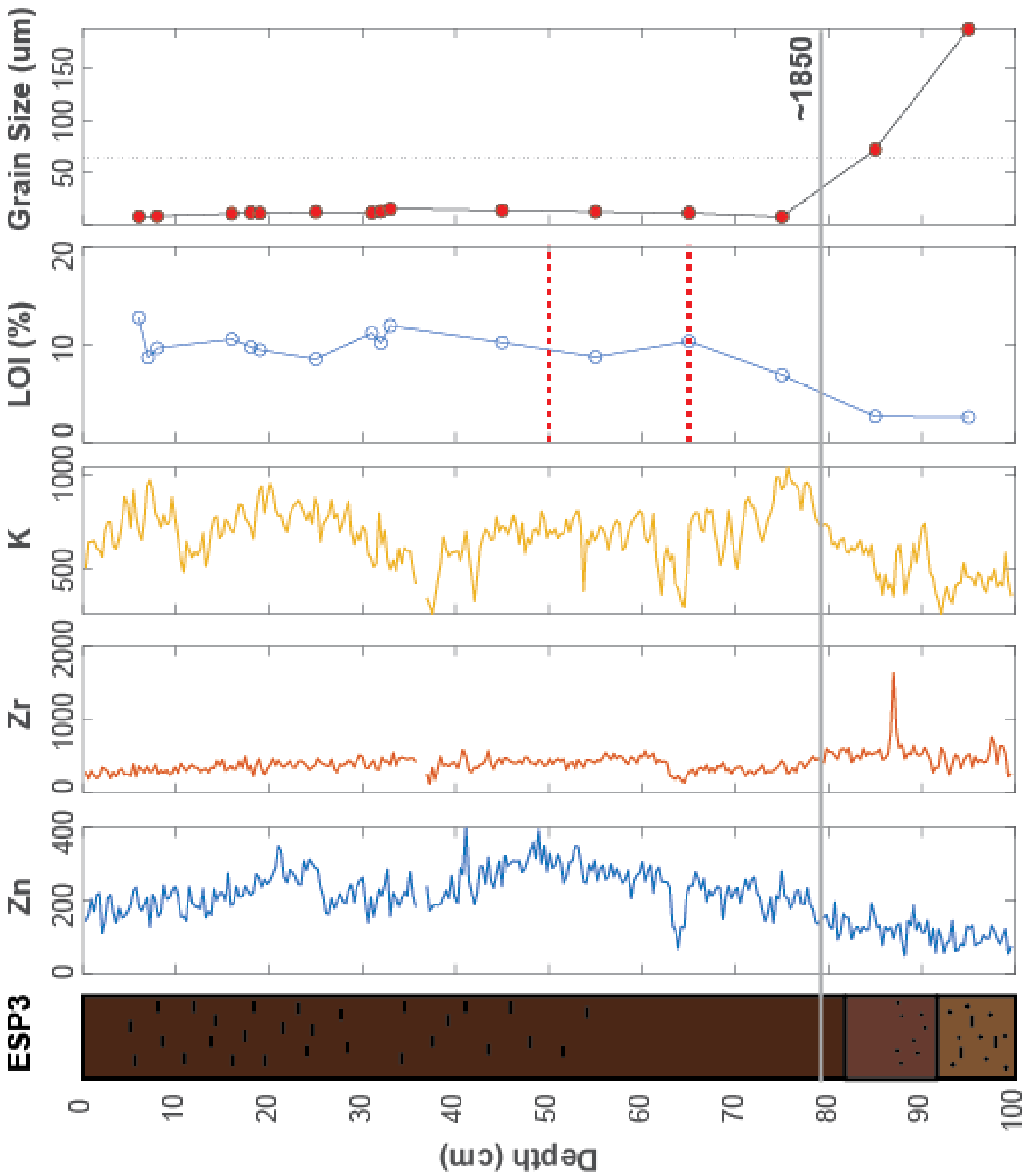

Figure 14 Transect of cores from Esopus Marsh. *Top:* ESP3, 2, 4, and 1 showing Zn XRF data, LOI (%), and grain size (µm) from left to right for each core. *Bottom:* ESP3, the longest core, from left to right showing an lithologic sketch, elemental data of Zn, Zr, K, LOI (%), and grain size (µm). The red dotted lines on the LOI plot mark the onset and peak of ^{137}Cs. The vertical dashed line on the grain size plots is at 63 µm, the distinction between sand and silt. The grey line on the bottom figure marks the change in environment at 1880, placed based on the sharp decrease in grain size.

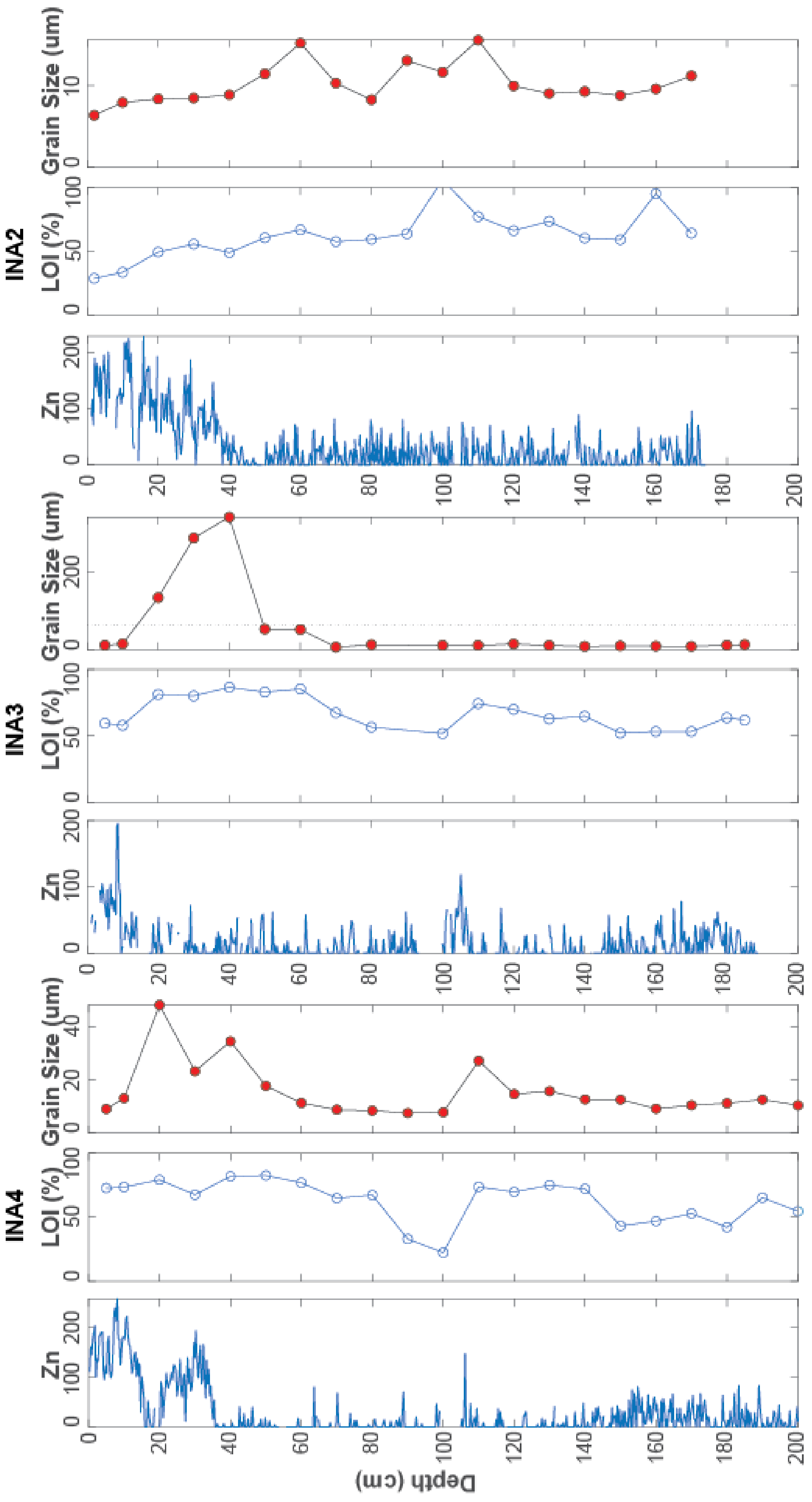
INA2
Grain Size (um)
0
10
LOI (%)
0
50
100
Zn
0
100
200
INA3
Grain Size (um)
0
200
LOI (%)
0
50
100
Zn
0
100
200
INA4
Grain Size (um)
0
20
40
LOI (%)
0
50
100
Zn
0
100
200
0
20
40
60
80
100
120
140
160
180
200
Depth (cm)

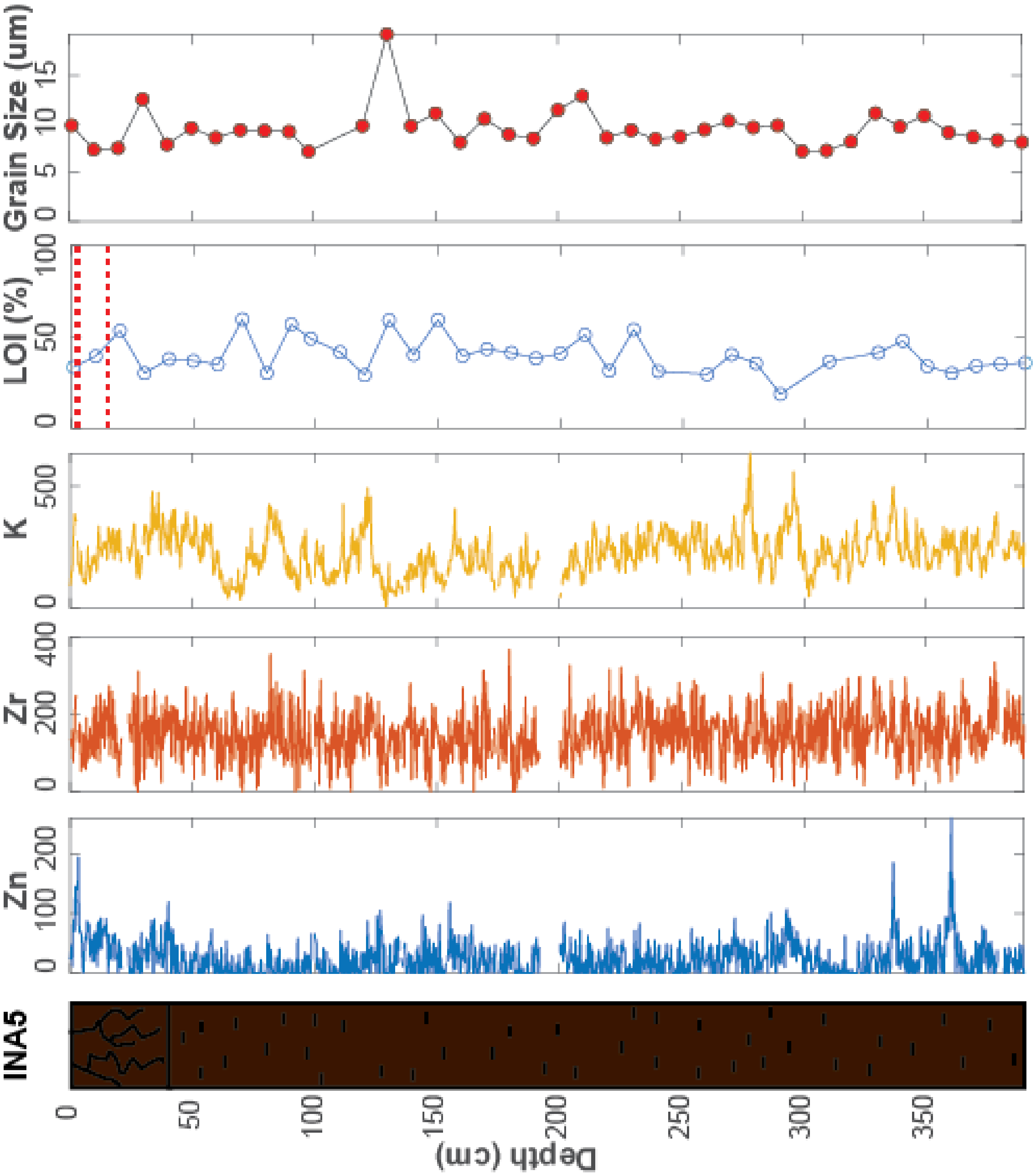

Figure 15 Transect of cores from Iona Island. *Top:* INA4, 3, and 2 showing Zn XRF data, LOI (%), and grain size (µm) from left to right for each core. *Bottom*: INA5, the longest core, from left to right showing an lithologic sketch, elemental data of Zn, Zr, K, LOI (%), and grain size (µm). The red dotted lines on the LOI plot mark the onset and peak of ^{137}Cs. The vertical dashed line on the grain size plots is at 63 µm, the distinction between sand and silt.

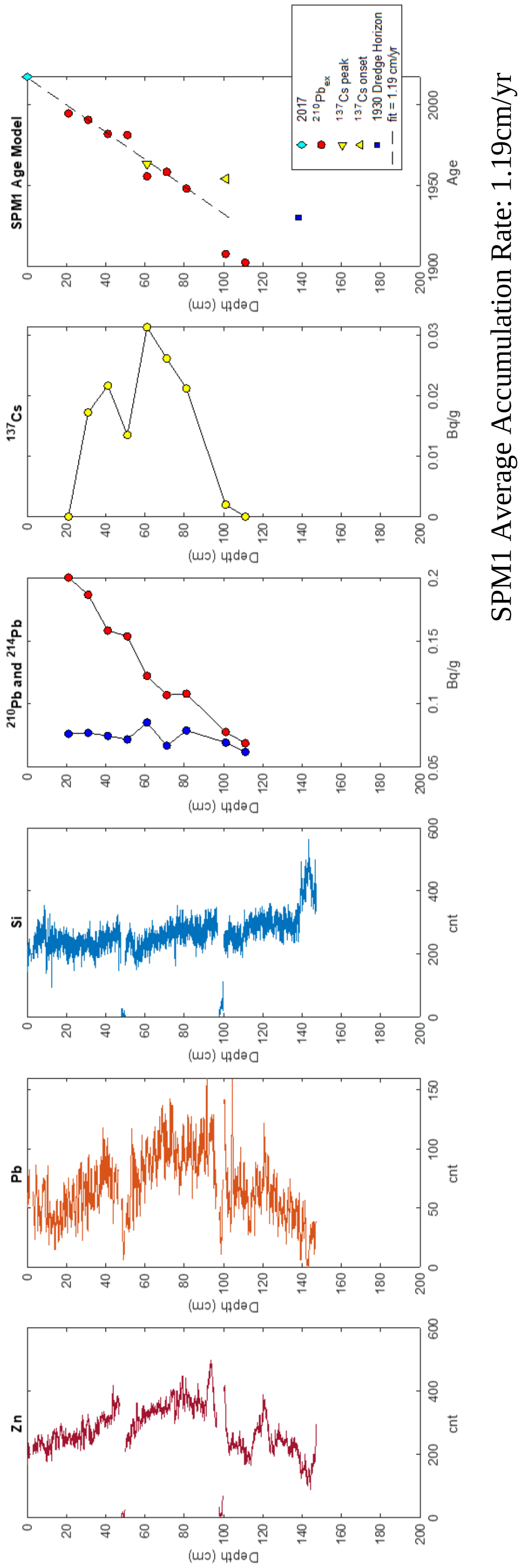

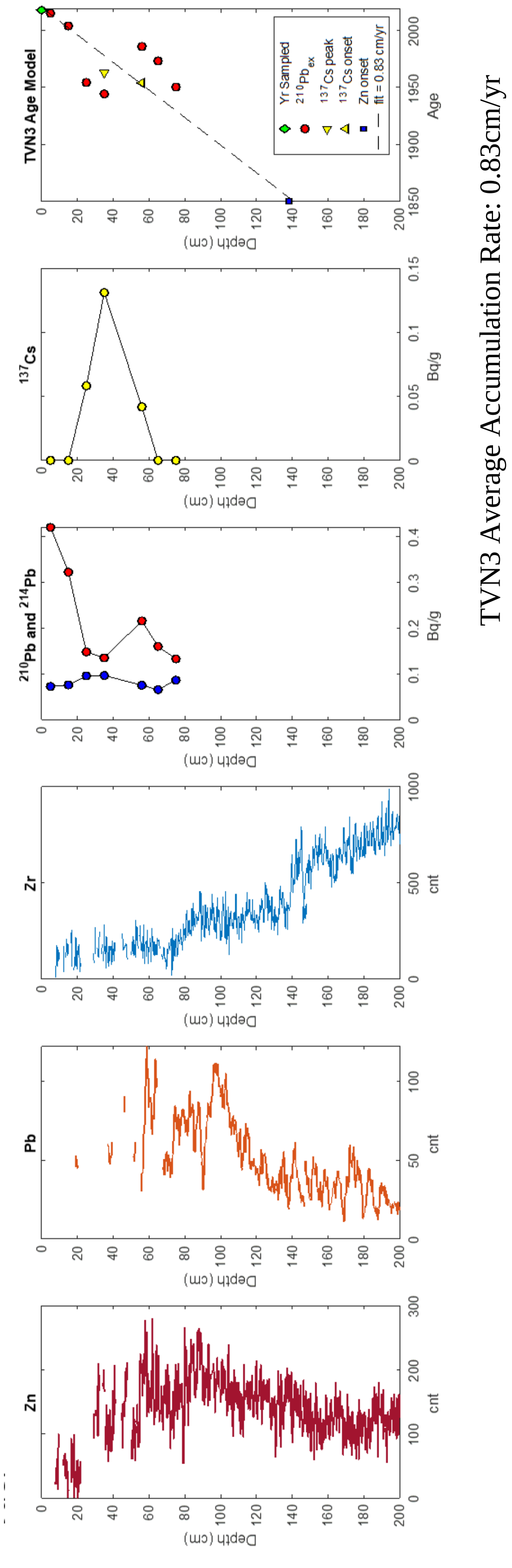

Figure 16 *SPM1 from left to right*- XRF data (Zn, Pb, and Zr), gamma spectroscopy results for ^{210}Pb, ^{214}Pb, and ^{137}Cs, and the compiled age model from the data points in the legend.

Figure 17 *TVN3 from left to right*- XRF data (Zn, Pb, and Zr), gamma spectroscopy results for ^{210}Pb, ^{214}Pb, and ^{137}Cs, and the compiled age model from the data points in the legend.

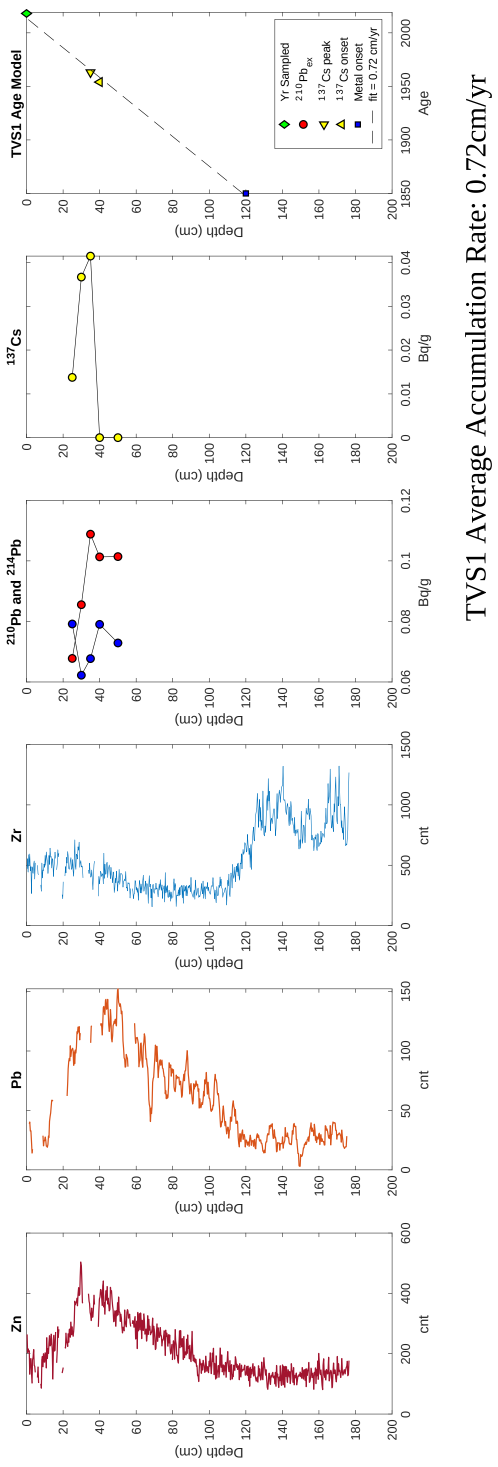

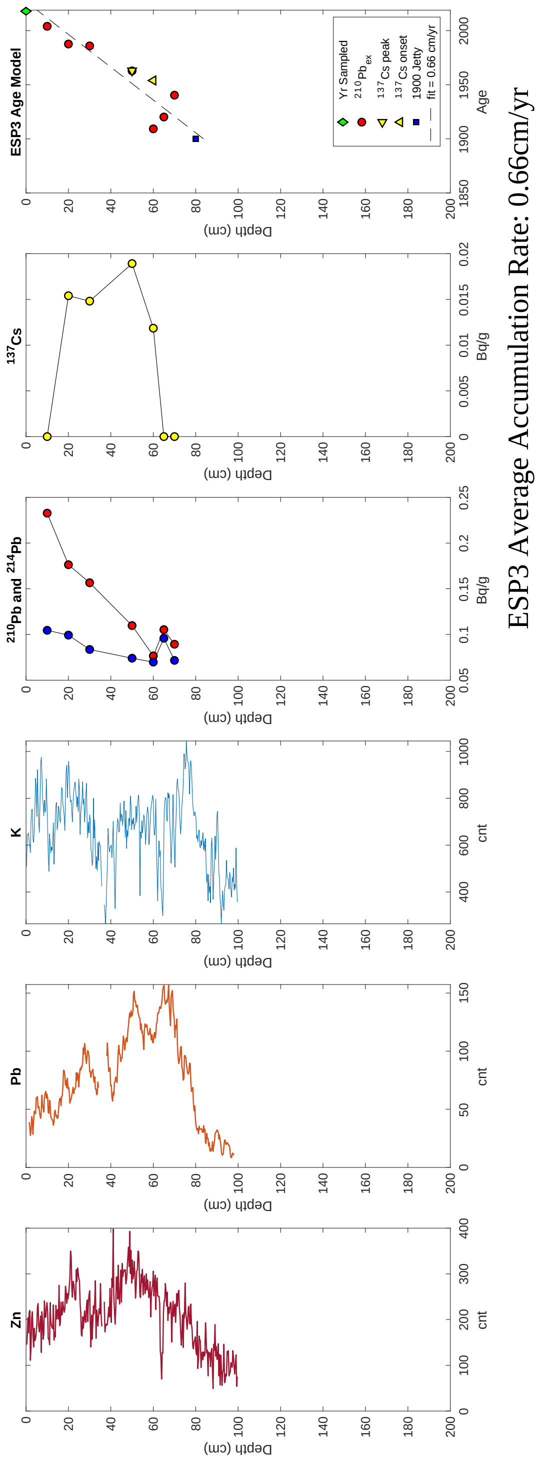

Figure 18 *TVS1 from left to right*- XRF data (Zn, Pb, and Zr), gamma spectroscopy results for ^{210}Pb, ^{214}Pb, and ^{137}Cs, and the compiled age model from the data points in the legend.

Figure 19 *ESP3 from left to right*- XRF data (Zn, Pb, and Zr), gamma spectroscopy results for ^{210}Pb, ^{214}Pb, and ^{137}Cs, and the compiled age model from the data points in the legend.

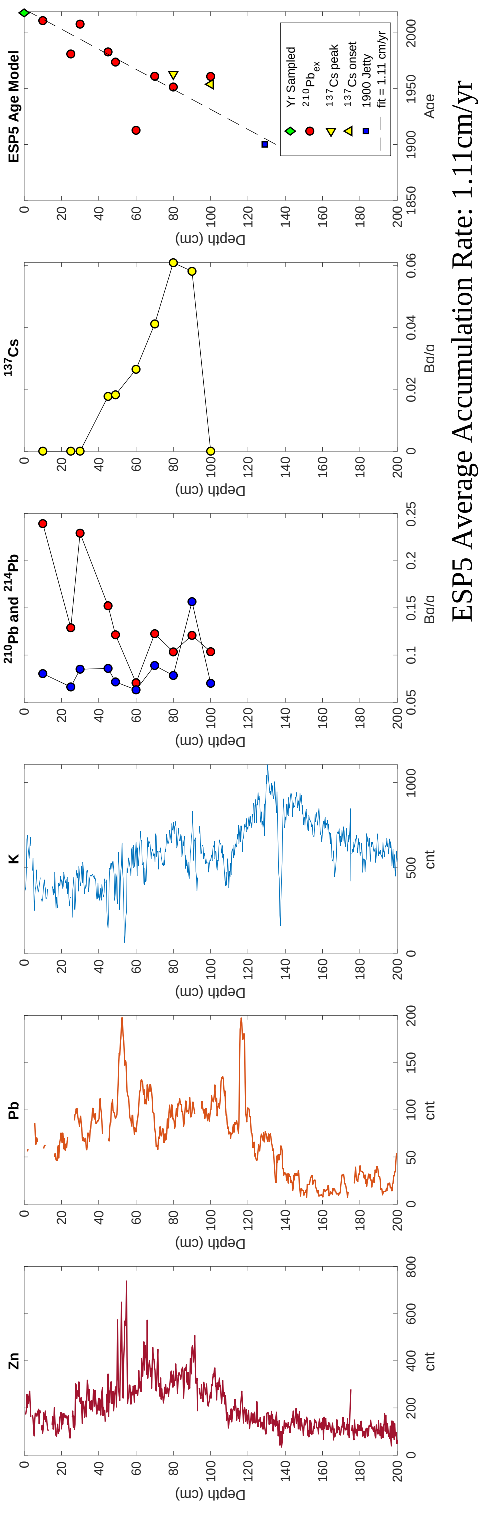

Figure 20 *ESP5 from left to right*- XRF data (Zn, Pb, and Zr), gamma spectroscopy results for ^{210}Pb, ^{214}Pb, and ^{137}Cs, and the compiled age model from the data points in the legend.

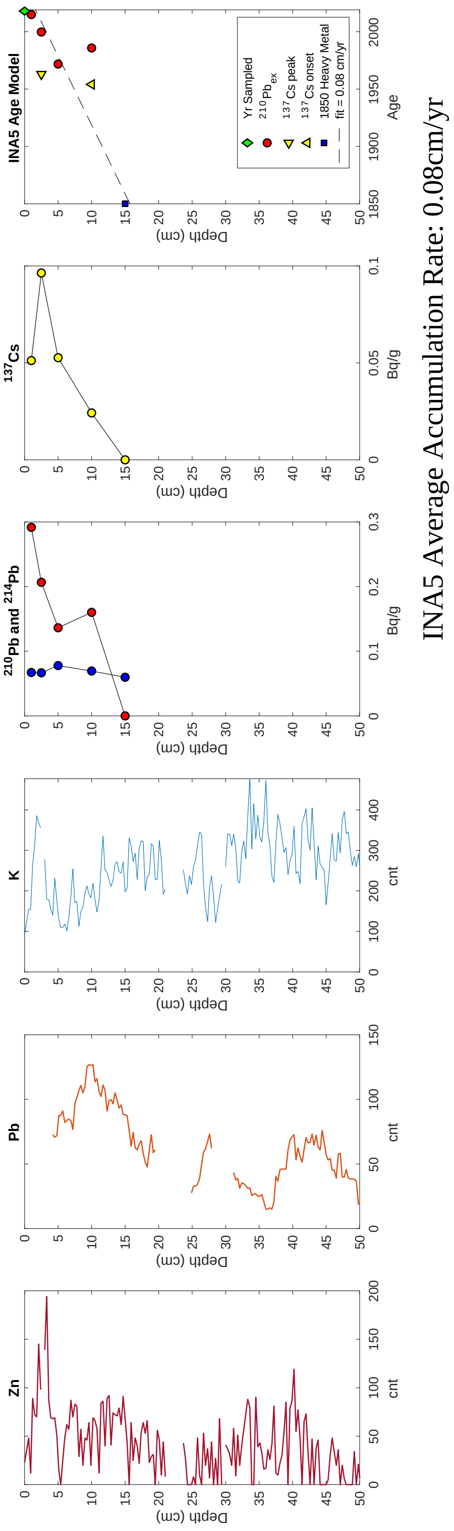

Figure 21 *INA5 from left to right*- XRF data (Zn, Pb, and Zr), gamma spectroscopy results for ^{210}Pb, ^{214}Pb, and ^{137}Cs, and the compiled age model from the data points in the legend.

APPENDIX

Table 6 Summary of core locations, and each drive at coring sites. The core type is noted next to site (RC is the 0.5-m Russian peat core, EX is the 1-m gauge core, and PPC is piston push coring).

Site & Core Type	**Latitude**	**Longitude**	**Start Depth (cm)**	**End Depth (cm)**
SPM1 RC	42.2996	-73.7755	0	50
SPM1 RC			50	100
SPM1 RC			100	150
SPM4 RC	42.3008	-73.7745	0	50
SPM4 RC			25	75
SPM4 RC			50	100
SPM4 RC			75	125
SPM7 RC	42.3022	-73.7756	0	50
SPM7 RC			25	75
SPM7 RC			50	100
SPM7 RC			75	125
TVN1 RC	42.042	-73.9207	0	50
TVN1 RC			50	100
TVN1 RC			100	150
TVN1 EX			0	57
TVN1 EX			100	200
TVN1 EX			135	185
TVN1 EX			200	265
TVN2 RC	42.0429	-73.9233	7	57
TVN2 EX			50	150
TVN2 EX			133	233
TVN3 RC	42.0427	-73.9222	5	55
TVN3 EX			50	150
TVN3 EX			145	245
TVN4 RC	42.0425	-73.9196	0	50
TVN4 RC			50	100
TVN4 RC			100	150
TVN4 EX			150	250
TVN4 EX			212	312
TVN5 RC	42.0427	-73.9184	0	50
TVN5 EX			0	50
TVN5 EX			50	150
TVN5 EX			147	247
TVS1 D1 PPC	42.0179	-73.9252	0	180
TVS1 D2 PPC			175	350
TVS2 D1 PPC	42.0182	-73.9221	0	160

TVS2 D2 PPC			186	345
TVS3 D1 PPC	42.0182	-73.9197	0	140
ESP1 EX	42.0703	-73.9324	0	100
ESP1 RC			0	50
ESP2 EX	42.0701	-73.9339	0	100
ESP3 EX	42.0701	-73.9342	0	100
ESP4 EX	42.0707	-73.933	0	80
ESP4 RC			50	100
ESP4 RC			100	150
ESP4 RC			150	200
ESP5 EX	42.0729	-73.9397	0	94
ESP5 EX			75	175
ESP5 RC			175	225
ESP5 RC			225	275
ESP5 RC			275	325
ESP5 RC			325	375
ESP5 RC			375	425
INA1 EX	41.2978	-73.9771	0	75
INA1 EX			50	150
INA2 EX	41.2998	-73.983	0	86
INA2 EX			75	175
INA3 EX	41.2982	-73.9826	0	95
INA3 EX			100	190
INA4 EX	41.2965	-73.983	0	100
INA4 EX			105	195
INA5 EX	41.2965	-73.983	0	100
INA5 EX			100	190
INA5 EX			200	300
INA5 EX			300	390
INA6 RC	41.3015	-73.9788	0	50
INA6 EX			50	140
INA6 EX			100	200
INA7 EX	41.3023	-73.9842	0	90
INA 7 EX			105	205

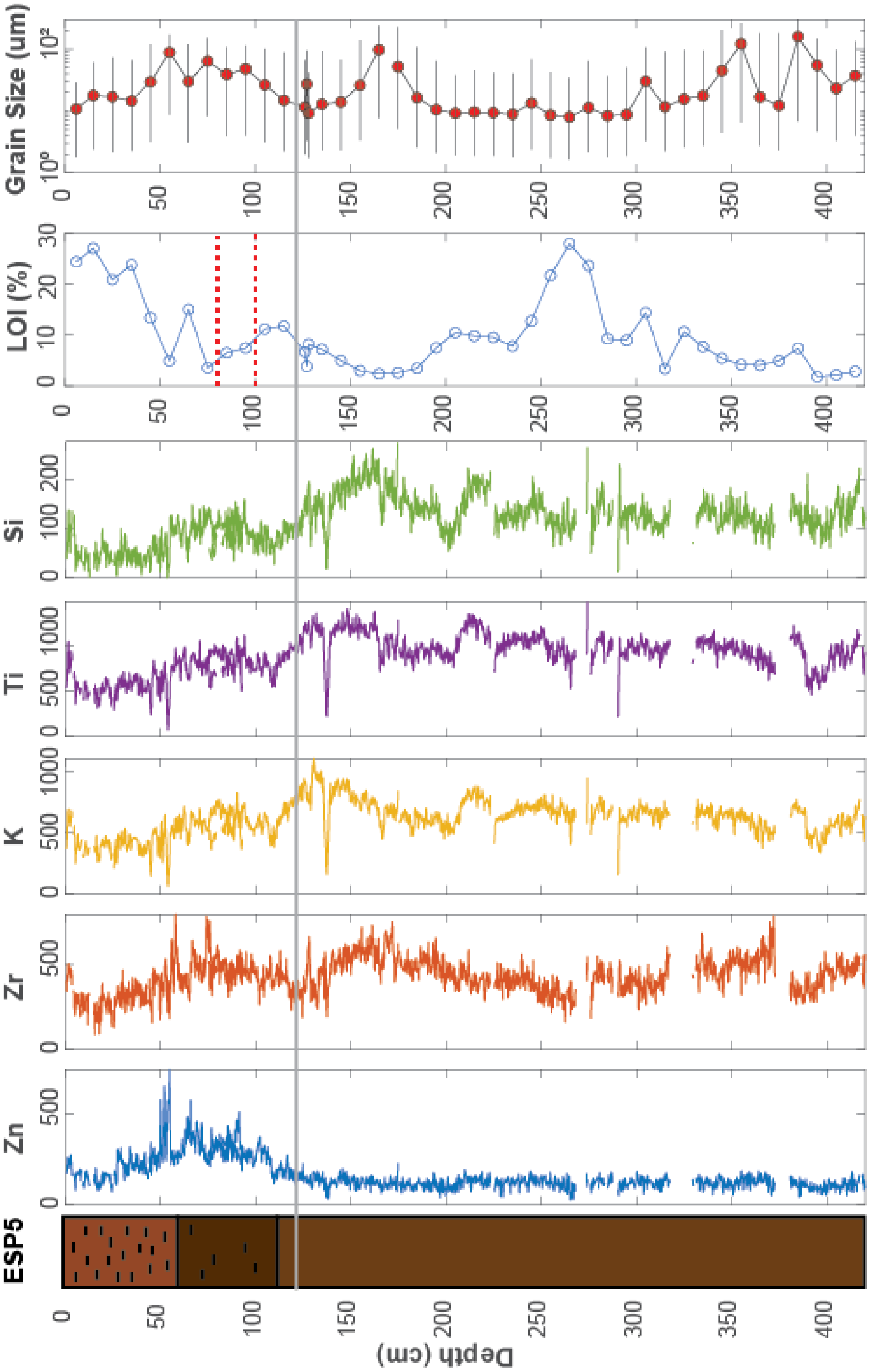

Figure 22 ESP5, the longest core, from left to right showing an lithologic sketch, elemental data of Zn, Zr, K, LOI (%), and grain size (µm). The red dotted lines on the LOI plot mark the onset and peak of ^{137}Cs. The vertical dashed line on the grain size plots is at 63 µm, the distinction between sand and silt. The grey line on the bottom figure marks the change in environment at 1850, placed based on the sharp decrease in grain size.

BIBLIOGRAPHY

Abood, K.A., 1974, CIRCULATION IN THE HUDSON ESTUARY: Annals of the New York Academy of Sciences, v. 250, p. 39–111, doi:10.1111/j.1749-6632.1974.tb43895.x.

Aggarwala, R., 1993, The Hudson River Railroad and the Development of Irvington, New York, 1849-1860, *in* The Hudson Valley Regional Review, p. 51–80.

Baranes, H., Woodruff, J.D., Loveless, J.P., and Hyodo, M., 2018, Interseismic Coupling-Based Earthquake and Tsunami Scenarios for the Nankai Trough: Geophysical Research Letters, v. 45, p. 2986–2994, doi:10.1002/2018GL077329.

Baranes, H.E., Woodruff, J.D., Wallace, D.J., Kanamaru, K., and Cook, T.L., 2016, Sedimentological records of the C.E. 1707 Hōei Nankai Trough tsunami in the Bungo Channel, southwestern Japan: Natural Hazards, v. 84, p. 1185–1205, doi:10.1007/s11069-016-2498-3.

Barbier, E.B., Hacker, S.D., Kennedy, C., Koch, E.W., Stier, A.C., and Silliman, B.R., 2011, The value of estuarine and coastal ecosystem services: Ecological Monographs, v. 81, p. 169–193, doi:10.1890/10-1510.1.

Benoit, G., Wang, E.X., Nieder, W.C., Levandowsky, M., and Breslin, V.T., 1999, Sources and history of heavy metal contamination and sediment deposition in Tivoli South Bay, Hudson River, New York: Estuaries, v. 22, p. 167–178, doi:10.2307/1352974.

Bowen, H.J.M., 1956, Strontium and barium in sea water and marine organisms: Journal of the Marine Biological Association of the United Kingdom, v. 35, p. 451–460, doi:10.1017/S0025315400010298.

Boyle, J.F., 2000, Rapid elemental analysis of sediment samples by isotope source XRF: , p. 10.

Brandon, C.M., Woodruff, J.D., Donnelly, J.P., and Sullivan, R.M., 2015, How Unique was Hurricane Sandy? Sedimentary Reconstructions of Extreme Flooding from New York Harbor: Scientific Reports, v. 4, doi:10.1038/srep07366.

Brandon, C.M., Woodruff, J.D., Lane, D.P., and Donnelly, J.P., 2013, Tropical cyclone wind speed constraints from resultant storm surge deposition: A 2500 year reconstruction of hurricane activity from St. Marks, FL: Geochemistry, Geophysics, Geosystems, v. 14, p. 2993–3008, doi:10.1002/ggge.20217.

Casagrande, D.J., Siefert, K., Berschinski, C., and Sutton, N., 1977, Sulfur in peat-forming systems of the Okefenokee Swamp and Florida Everglades: origins of sulfur in coal: Geochimica et Cosmochimica Acta, v. 41, p. 161–167, doi:10.1016/0016-7037(77)90196-X.

Chagué-Goff, C., 2010, Chemical signatures of palaeotsunamis: A forgotten proxy? Marine Geology, v. 271, p. 67–71, doi:10.1016/j.margeo.2010.01.010.

Chagué-Goff, C., Andrew, A., Szczuciński, W., Goff, J., and Nishimura, Y., 2012, Geochemical signatures up to the maximum inundation of the 2011 Tohoku-oki tsunami —

Implications for the 869AD Jogan and other palaeotsunamis: Sedimentary Geology, v. 282, p. 65–77, doi:10.1016/j.sedgeo.2012.05.021.

Chaumillon, E. et al., 2017, Storm-induced marine flooding: Lessons from a multidisciplinary approach: Earth-Science Reviews, v. 165, p. 151–184, doi:10.1016/j.earscirev.2016.12.005.

Chen, Z., Chen, Z., and Zhang, W., 1997, Quaternary Stratigraphy and Trace-Element Indices of the Yangtze Delta, Eastern China, with Special Reference to Marine Transgressions: Quaternary Research, v. 47, p. 181–191, doi:10.1006/qres.1996.1878.

Chou, C., 2010, MACROFOSSIL EVIDENCE FOR MIDDLE TO LATE HOLOCENE VEGETATION SHIFTS AT IONA ISLAND MARSH, HUDSON VALLEY, NY: Columbia University, 34 p.

Chu, J.-H., Sampson, C.R., Levine, A.S., and Fukada, E., 2002, The joint typhoon warning center tropical cyclone best-tracks, 1945–2000: Ref. NRL/MR/7540-02, v. 16, http://www.metoc.navy.mil/jtwc/products/best-tracks/tc-bt-report.html (accessed February 2019).

Collins, M.J., and Miller, D., 2012, Upper Hudson River Estuary (usa) Floodplain Change Over the 20th Century: River Research and Applications, v. 28, p. 1246–1253, doi:10.1002/rra.1509.

Cook, T.L., Yellen, B.C., Woodruff, J.D., and Miller, D., 2015, Contrasting human versus climatic impacts on erosion: Geophysical Research Letters, v. 42, p. 6680–6687, doi:10.1002/2015GL064436.

Craft, C., Clough, J., Ehman, J., Joye, S., Park, R., Pennings, S., Guo, H., and Machmuller, M., 2009, Forecasting the effects of accelerated sea-level rise on tidal marsh ecosystem services: Frontiers in Ecology and the Environment, v. 7, p. 73–78, doi:10.1890/070219.

Croudace, I.W., Rindby, A., and Rothwell, R.G., 2006, ITRAX: description and evaluation of a new multi-function X-ray core scanner: Geological Society, London, Special Publications, v. 267, p. 51–63, doi:10.1144/GSL.SP.2006.267.01.04.

Croudace, I.W., and Rothwell, R.G., 2015, Micro-XRF studies of sediment cores: Springer, Developments in Paleoenvironmental Research, v. 17.

Fox, G.A., Sheshukov, A., Cruse, R., Kolar, R.L., Guertault, L., Gesch, K.R., and Dutnell, R.C., 2016, Reservoir Sedimentation and Upstream Sediment Sources: Perspectives and Future Research Needs on Streambank and Gully Erosion: Environmental Management, v. 57, p. 945–955, doi:10.1007/s00267-016-0671-9.

Fukumoto, Y., 2011, Mid-late Holocene paleoenvironment in Karako lowland, western Japan, inferred from diatom analysis: Quaternary International, v. 230, p. 115–121, doi:10.1016/j.quaint.2010.08.003.

Furumoto K., Takemoto Y., Makita H., and Tateishi H., 1999, THE CHANGE OF THE WATER QUALITY AND NUTRIENT RELEASE FROM BOTTOM SEDIMENT IN

KAWAHARA LAKE: PROCEEDINGS OF HYDRAULIC ENGINEERING, v. 43, p. 1001–1006, doi:10.2208/prohe.43.1001.

Geological Survey of Japan, 2017, Online Geological Map of Japan:, https://www.gsj.jp/en/education/geomap-e/online-map.html (accessed January 2019).

Goff, J., McFadgen, B.G., and Chagué-Goff, C., 2004, Sedimentary differences between the 2002 Easter storm and the 15th-century Okoropunga tsunami, southeastern North Island, New Zealand: Marine Geology, v. 204, p. 235–250, doi:10.1016/S0025-3227(03)00352-9.

Goslin, J., and Clemmensen, L.B., 2017, Proxy records of Holocene storm events in coastal barrier systems: Storm-wave induced markers: Quaternary Science Reviews, v. 174, p. 80–119, doi:10.1016/j.quascirev.2017.08.026.

Goto, T., Satake, K., Sugai, T., Ishibe, T., Harada, T., and Gusman, A.R., 2017, Effects of topography on particle composition of 2011 tsunami deposits on the ria-type Sanriku coast, Japan: Quaternary International, v. 456, p. 17–27, doi:10.1016/j.quaint.2017.05.014.

Goto, T., Satake, K., Sugai, T., Ishibe, T., Harada, T., and Murotani, S., 2015, Historical tsunami and storm deposits during the last five centuries on the Sanriku coast, Japan: Marine Geology, v. 367, p. 105–117, doi:10.1016/j.margeo.2015.05.009.

Hartig, E.K., Gornitz, V., Kolker, A., Mushacke, F., and Fallon, D., 2002, Anthropogenic and climate-change impacts on salt marshes of Jamaica Bay, New York City: Wetlands, v. 22, p. 71–89, doi:10.1672/0277-5212(2002)022[0071:AACCIO]2.0.CO;2.

Haslett, J., and Parnell, A., 2008, A Simple Monotone Process with Application to Radiocarbon-Dated Depth Chronologies: Journal of the Royal Statistical Society. Series C (Applied Statistics), v. 57, p. 399–418.

Haug, G.H., Günther, D., Peterson, L.C., Sigman, D.M., Hughen, K.A., and Aeschlimann, B., 2003, Climate and the Collapse of Maya Civilization: Science, v. 299, p. 1731–1735, doi:10.1126/science.1080444.

Haug, G.H., Hughen, K.A., Sigman, D.M., Peterson, L.C., and Röhl, U., 2001, Southward Migration of the Intertropical Convergence Zone Through the Holocene: Science, v. 293, p. 1304–1308, doi:10.1126/science.1059725.

Heiri, O., Lotter, A.F., and Lemcke, G., 2001, Loss on ignition as a method for estimating organic and carbonate content in sediments: reproducibility and comparability of results: Journal of Paleolimnology, v. 25, p. 101–110, doi:10.1023/A:1008119611481.

Hoshizumi, H., Uto, K., and Watanabe, K., 1999, Geology and eruptive history of Unzen volcano, Shimabara Peninsula, Kyushu, SW Japan: Journal of Volcanology and Geothermal Research, v. 89, p. 81–94, doi:10.1016/S0377-0273(98)00125-5.

Hossain, Md.M., Perhar, G., Arhonditsis, G.B., Matsuishi, T., Goto, A., and Azuma, M., 2013, Examination of the effects of largemouth bass (Micropterus salmoides) and bluegill (Lepomis macrochirus) on the ecosystem attributes of lake Kawahara-oike, Nagasaki, Japan: Ecological Informatics, v. 18, p. 149–161, doi:10.1016/j.ecoinf.2013.07.005.

Comprehensive Restoration Plan for HRE, 2016, https://www.nan.usace.army.mil/Missions/Environmental/Comprehensive-Restoration-Plan-for-the-Hudson-Raritan-Estuary/ (accessed April 2019).

Japan Meteorological Agency, 2013, Lessons learned from the tsunami disaster caused by the 2011 Great East Japan Earthwauke and improvements in JMA’s tsunami warning system.:, https://www.jma.go.jp/jma/en/Publications/publications.html (accessed February 2019).

Kemp, A.C., Horton, B.P., Nikitina, D., Vane, C.H., Potapova, M., Weber-Bruya, E., Culver, S.J., Repkina, T., and Hill, D.F., 2017, The distribution and utility of sea-level indicators in Eurasian sub-Arctic salt marshes (White Sea, Russia): Boreas, v. 46, p. 562–584, doi:10.1111/bor.12233.

Kimura, J., Staniforth, M., Lien, L.T., and Sasaki, R., 2014, Naval Battlefield Archaeology of the Lost Kublai Khan Fleets: Naval Battlefield Archaeology of the Kublai Khan Fleets: International Journal of Nautical Archaeology, v. 43, p. 76–86, doi:10.1111/1095-9270.12033.

Koinig, K.A., Shotyk, W., Lotter, A.F., Ohlendorf, C., and Sturm, M., 2003, 9000 years of geochemical evolution of lithogenic major and trace elements in the sediment of an alpine lake – the role of climate, vegetation, and land-use history: Journal of Paleolimnology, v. 30, p. 307–320, doi:10.1023/A:1026080712312.

Komatsubara, J., and Fujiwara, O., 2007, Overview of Holocene Tsunami Deposits along the Nankai, Suruga, and Sagami Troughs, Southwest Japan, *in* Satake, K., Okal, E.A., and Borrero, J.C. eds., Tsunami and Its Hazards in the Indian and Pacific Oceans, Birkhäuser Basel, Pageoph Topical Volumes, p. 493–507.

Komatsubara, J., Fujiwara, O., Takada, K., Sawai, Y., Aung, T.T., and Kamataki, T., 2008, Historical tsunamis and storms recorded in a coastal lowland, Shizuoka Prefecture, along the Pacific Coast of Japan: Sedimentology, v. 55, p. 1703–1716, doi:10.1111/j.1365-3091.2008.00964.x.

Kortekaas, S., and Dawson, A.G., 2007, Distinguishing tsunami and storm deposits: An example from Martinhal, SW Portugal: Sedimentary Geology, v. 200, p. 208–221, doi:10.1016/j.sedgeo.2007.01.004.

Kurnio, H., and Aryanto, N.C.D., 2010, PALEO-CHANNELS OF SINGKAWANG WATERS WEST KALIMANTAN AND ITS REL ATION TO THE OCCURRENCES OF SUB-SEABOT TOM GOLD PL ACERS BASED ON STRATA BOX SEISMIC RECORD ANALYSES: v. 25, p. 12.

Landsea, C.W., Anderson, C., Charles, N., Clark, G., Dunion, J., Fernandes-Partagas, J., Hungerford, P., Neumann, C., and Zimmer, M., 2004, The Atlantic hurricane database re-analysis project: Documentation for the 1851–1910 alterations and additions to the HURDAT database, *in* Murnane, R. and Liu, K. eds., Hurricanes and Typhoons: Past, Present and Future, New York, Columbia University Press, p. 177–221.

Milliman, J.D., and Farnsworth, K.L., 2011, Runoff, erosion, and delivery to the coastal ocean: River discharge to the coastal ocean: a global synthesis, Cambridge University Press, Cambridge, UK, p. 13–69.

Morton, R.A., Gelfenbaum, G., and Jaffe, B.E., 2007, Physical criteria for distinguishing sandy tsunami and storm deposits using modern examples: Sedimentary Geology, v. 200, p. 184–207, doi:10.1016/j.sedgeo.2007.01.003.

Nakada, M., Maeda, Y., Nagaoka, S., Yokoyama, Y., Okuno, J., Matsumoto, E., Matsushima, Y., Sato, H., Matsuda, I., and Sampei, Y., 1994, Glacio-hydro-isostasy and Underwater Jomon Sites along the West Coast of Kyushu, Japan: The Quaternary Research (Daiyonki-Kenkyu), v. 33, p. 361–368, doi:10.4116/jaqua.33.361.

Nanayama, F., Shigeno, K., Satake, K., Shimokawa, K., Koitabashi, S., Miyasaka, S., and Ishii, M., 2000, Sedimentary differences between the 1993 Hokkaido-nansei-oki tsunami and the 1959 Miyakojima typhoon at Taisei, southwestern Hokkaido, northern Japan: Sedimentary Geology, v. 135, p. 255–264, doi:10.1016/S0037-0738(00)00076-2.

Neumann, J., 1975, great historical events that were significantly affected by the weather: I. the Mongol invasions of Japan: Bulletin of the American Meteorological Society, v. 56, p. 1167–1171, doi:10.1175/1520-0477(1975)056<1167:GHETWS>2.0.CO;2.

Nitsche, F.O., Kenna, T.C., and Haberman, M., 2010, Quantifying 20th century deposition in complex estuarine environment: An example from the Hudson River: Estuarine, Coastal and Shelf Science, v. 89, p. 163–174, doi:10.1016/j.ecss.2010.06.011.

Normile, D., 2011, Scientific Consensus on Great Quake Came Too Late: Science, v. 332, p. 22–23, doi:10.1126/science.332.6025.22.

Parnell, A.C., Haslett, J., Allen, J.R.M., Buck, C.E., and Huntley, B., 2008, A flexible approach to assessing synchroneity of past events using Bayesian reconstructions of sedimentation history: Quaternary Science Reviews, v. 27, p. 1872–1885, doi:10.1016/j.quascirev.2008.07.009.

Pederson, D.C., Peteet, D.M., Kurdyla, D., and Guilderson, T., 2005, Medieval Warming, Little Ice Age, and European impact on the environment during the last millennium in the lower Hudson Valley, New York, USA: Quaternary Research, v. 63, p. 238–249, doi:10.1016/j.yqres.2005.01.001.

Pennington, W., Tutin, T.G., Cambray, R.S., and Fisher, E.M., 1973, Observations on Lake Sediments using Fallout 137Cs as a Tracer: Nature, v. 242, p. 324–326, doi:10.1038/242324a0.

Peteet, D.M., Nichols, J., Kenna, T., Chang, C., Browne, J., Reza, M., Kovari, S., Liberman, L., and Stern-Protz, S., 2018, Sediment starvation destroys New York City marshes' resistance to sea level rise: Proceedings of the National Academy of Sciences, v. 115, p. 10281–10286, doi:10.1073/pnas.1715392115.

Peterson, L.C., and Haug, G.H., 2006, Variability in the mean latitude of the Atlantic Intertropical Convergence Zone as recorded by riverine input of sediments to the Cariaco Basin

(Venezuela): Palaeogeography, Palaeoclimatology, Palaeoecology, v. 234, p. 97–113, doi:10.1016/j.palaeo.2005.10.021.

Peterson, L.C., Haug, G.H., Hughen, K.A., and Röhl, U., 2000, Rapid Changes in the Hydrologic Cycle of the Tropical Atlantic During the Last Glacial: Science, v. 290, p. 1947–1951, doi:10.1126/science.290.5498.1947.

Ralston, D.K., Talke, S., Geyer, W.R., Al'Zubadaei, H., and Sommerfield, C.K., 2018, Bigger tides, less flooding: Effects of dredging on barotropic dynamics in a highly modified estuary: Journal of Geophysical Research: Oceans, doi:10.1029/2018JC014313.

Ralston, D.K., Warner, J.C., Geyer, W.R., and Wall, G.R., 2013, Sediment transport due to extreme events: The Hudson River estuary after tropical storms Irene and Lee: Geophysical Research Letters, v. 40, p. 5451–5455, doi:10.1002/2013GL057906.

Redfield, A.C., 1972, Development of a New England Salt Marsh: Ecological Monographs, v. 42, p. 201–237, doi:10.2307/1942263.

Reimer, P.J. et al., 2013, IntCal13 and Marine13 Radiocarbon Age Calibration Curves 0–50,000 Years cal BP: Radiocarbon, v. 55, p. 1869–1887, doi:10.2458/azu_js_rc.55.16947.

Ritchie, J.C., and McHenry, J.R., 1990, Application of Radioactive Fallout Cesium-137 for Measuring Soil Erosion and Sediment Accumulation Rates and Patterns: A Review: Journal of Environmental Quality, v. 19, p. 215–233, doi:10.2134/jeq1990.00472425001900020006x.

Rossabi, M., 2009, Khubilai Khan: His Life and Times: Univ of California Press, 350 p.

Sasaki, R.J., 2015, The Origins of the Lost Fleet of the Mongol Empire: Texas A&M University Press, 217 p.

Sasaki, H., and Yamakawa, S., 2007, Natural Hazards in Japan, *in* Lidstone, J., Dechano, L.M., and Stoltman, J.P. eds., International Perspectives on Natural Disasters: Occurrence, Mitigation, and Consequences, Dordrecht, Springer Netherlands, p. 163–180, doi:10.1007/978-1-4020-2851-9_8.

Sato, H., 2001, Holocene uplift derived from relative sea-level records along the coast of western Kobe, Japan: Quaternary Science Reviews, v. 20, p. 1459–1474, doi:10.1016/S0277-3791(01)00005-1.

Sawai, Y. et al., 2009, Aperiodic recurrence of geologically recorded tsunamis during the past 5500 years in eastern Hokkaido, Japan: Journal of Geophysical Research: Solid Earth, v. 114, doi:10.1029/2007JB005503.

Simpson, R.H., and Saffir, H., 1974, The hurricane disaster potential scale: Weatherwise, v. 27, p. 169.

Singh, A.K., Hasnain, S.I., and Banerjee, D.K., 1999, Grain size and geochemical partitioning of heavy metals in sediments of the Damodar River – a tributary of the lower Ganga, India: Environmental Geology, v. 39, p. 90–98, doi:10.1007/s002540050439.

Sritrairat, S., Peteet, D.M., Kenna, T.C., Sambrotto, R., Kurdyla, D., and Guilderson, T., 2012, A history of vegetation, sediment and nutrient dynamics at Tivoli North Bay, Hudson Estuary, New York: Estuarine, Coastal and Shelf Science, v. 102–103, p. 24–35, doi:10.1016/j.ecss.2012.03.003.

Suppasri, A., Shuto, N., Imamura, F., Koshimura, S., Mas, E., and Yalciner, A.C., 2013, Lessons Learned from the 2011 Great East Japan Tsunami: Performance of Tsunami Countermeasures, Coastal Buildings, and Tsunami Evacuation in Japan: Pure and Applied Geophysics, v. 170, p. 993–1018, doi:10.1007/s00024-012-0511-7.

Suzuki, A., Yokoyama, Y., Kan, H., Minoshima, K., Matsuzaki, H., Hamanaka, N., and Kawahata, H., 2008, Identification of 1771 Meiwa Tsunami deposits using a combination of radiocarbon dating and oxygen isotope microprofiling of emerged massive Porites boulders: Quaternary Geochronology, v. 3, p. 226–234, doi:10.1016/j.quageo.2007.12.002.

Tabak, N.M., Laba, M., and Spector, S., 2016, Simulating the Effects of Sea Level Rise on the Resilience and Migration of Tidal Wetlands along the Hudson River: PLOS ONE, v. 11, p. e0152437, doi:10.1371/journal.pone.0152437.

Taira, A., 2001, Tectonic Evolution of the Japanese Island Arc System: Annual Review of Earth and Planetary Sciences, v. 29, p. 109–134, doi:10.1146/annurev.earth.29.1.109.

Timeline – Saugerties Lighthouse, 2011, Saugerties Lighthouse, https://www.saugertieslighthouse.com/history/timeline/ (accessed April 2019).

Triplett, L., and Heck, J., 2013, LacCore Grain Size Pretreatment SOP:

Turnbull, S., 2013, The Mongol Invasions of Japan 1274 and 1281: Bloomsbury Publishing, 98 p.

Wall, G.R., Nystrom, E.A., and Litten, S., 2008, Suspended Sediment Transport in the Freshwater Reach of the Hudson River Estuary in Eastern New York: Estuaries and Coasts, v. 31, p. 542–553, doi:10.1007/s12237-008-9050-y.

Wallace, D.J., Woodruff, J.D., Anderson, J.B., and Donnelly, J.P., 2014, Palaeohurricane reconstructions from sedimentary archives along the Gulf of Mexico, Caribbean Sea and western North Atlantic Ocean margins: Geological Society, London, Special Publications, v. 388, p. 481–501, doi:10.1144/SP388.12.

Williams, S.C., Simpson, H.J., Olsen, C.R., and Bopp, R.F., 1978, Sources of heavy metals in sediments of the Hudson river Estuary: Marine Chemistry, v. 6, p. 195–213, doi:10.1016/0304-4203(78)90030-0.

Woodruff, J.D., Donnelly, J.P., and Okusu, A., 2009, Exploring typhoon variability over the mid-to-late Holocene: evidence of extreme coastal flooding from Kamikoshiki, Japan: Quaternary Science Reviews, v. 28, p. 1774–1785, doi:10.1016/j.quascirev.2009.02.005.

Woodruff, J.D., Geyer, W.R., Sommerfield, C.K., and Driscoll, N.W., 2001, Seasonal variation of sediment deposition in the Hudson River estuary: Marine Geology, v. 179, p. 105–119, doi:10.1016/S0025-3227(01)00182-7.

Woodruff, J.D., Irish, J.L., and Camargo, S.J., 2013a, Coastal flooding by tropical cyclones and sea-level rise: Nature, v. 504, p. 44–52, doi:10.1038/nature12855.

Woodruff, J.D., Kanamaru, K., Kundu, S., and Cook, T.L., 2015, Depositional evidence for the Kamikaze typhoons and links to changes in typhoon climatology: Geology, v. 43, p. 91–94, doi:10.1130/G36209.1.

Woodruff, J.D., Martini, A.P., Elzidani, E.Z.H., Naughton, T.J., Kekacs, D.J., and MacDonald, D.G., 2013b, Off-river waterbodies on tidal rivers: Human impact on rates of infilling and the accumulation of pollutants: Geomorphology, v. 184, p. 38–50, doi:10.1016/j.geomorph.2012.11.012.

Wright, L.D., 1977, Sediment transport and deposition at river mouths: A synthesis: GSA Bulletin, v. 88, p. 857–868, doi:10.1130/0016-7606(1977)88<857:STADAR>2.0.CO;2.

Yellen, B., and Steinschneider, S., 2019, Gradual recovery from flood distrubance recorded in sediment cores, *in* Portland, ME, Geological Society of America Abstracts with Programs, 1, v. 51, doi:10.1130/abs/2019NE-328688.

Yellen, B., Woodruff, J.D., Cook, T.L., and Newton, R.M., 2016, Historically unprecedented erosion from Tropical Storm Irene due to high antecedent precipitation: Earth Surface Processes and Landforms, v. 41, p. 677–684, doi:10.1002/esp.3896.

Yellen, B., Woodruff, J.D., Kratz, L.N., Mabee, S.B., Morrison, J., and Martini, A.M., 2014, Source, conveyance and fate of suspended sediments following Hurricane Irene. New England, USA: Geomorphology, v. 226, p. 124–134, doi:10.1016/j.geomorph.2014.07.028.

Yokoyama, Y., Nakada, M., Maeda, Y., Nagaoka, S., Okuno, J., Matsumoto, E., Sato, H., and Matsushima, Y., 1996, Holocene sea-level change and hydro-isostasy along the west coast of Kyushu, Japan: Palaeogeography, Palaeoclimatology, Palaeoecology, v. 123, p. 29–47, doi:10.1016/0031-0182(95)00112-3.

Yokoyama, Y., Okuno, J., Miyairi, Y., Obrochta, S., Demboya, N., Makino, Y., and Kawahata, H., 2012, Holocene sea-level change and Antarctic melting history derived from geological observations and geophysical modeling along the Shimokita Peninsula, northern Japan: HOLOCENE SEA LEVEL AND ANTARCTIC MELTING: Geophysical Research Letters, v. 39, p. n/a-n/a, doi:10.1029/2012GL051983.